Rational Design and Reticulation of Infinite qbe Rod Secondary Building Units into Metal-Organic Frameworks through a Global Desymmetrization Approach for Inverse C_3H_8/C_3H_6 Separation

Wei Gong,[*,a] Yi Xie,[b] Akihito Yamano,[e] Sho Ito,[e] Eric W. Reinheimer,[f] Jinqiao Dong,[a] Christos D. Malliakas,[b] Davide M. Proserpio,[d] Yong Cui,[a] and Omar K. Farha[b,c]

[a]School of Chemistry and Chemical Engineering, Frontiers Science Center for Transformative Molecules and State Key Laboratory of Metal Matrix Composites, Shanghai Jiao Tong University, Shanghai 200240, China

[b]Department of Chemistry and International Institute for Nanotechnology (IIN), Northwestern University, Evanston, Illinois 60208, United States

[c]Department of Chemical & Biological Engineering, Northwestern University, Evanston, Illinois 60208, United States

[d]Dipartimento di Chimica, Università degli studi di Milano, Milano, Italy

[e]Rigaku Corporation, 3-9-12 Matsubara-cho, Akishima, Tokyo 196-8666, Japan.

[f]Rigaku Americas Corporation, 9009 New Trails Drive, The Woodlands, Texas 77381, United States

Email: gongwei_2014jd@sjtu.edu.cn

1. Materials and General Procedures.

All the chemicals are commercially available and were used without further purification. Thermogravimetric analyses (TGA) were performed on a TGA/DCS 1 system (Mettler-Toledo, Columbus, OH) with STARe software. Samples were heated from 25 to 600 °C at a rate of 5 °C/min under N_2 with flow rate 20 mL/min. Powder X-ray diffraction (PXRD) data were collected on a STOE-STADI P powder diffractometer operating at 40 kV voltage and 40 mA current with Cu-Kα1 X-ray radiation (λ = 0.154056 nm) in transmission geometry. The calculated PXRD patterns were produced using the Mercury software and single crystal reflection data. ^{1}H NMR, and ^{13}C NMR experiments were carried out on a Bruker Avance III 500 MHz system. N_2 sorption isotherms were measured using a Micrometritics ASAP 2420 surface area analyzer at 77 K. Before the isotherm measurement, Cu-ASY, UMCM-150, and UMCM-151 were exchanged with methanol 3 times (6 h for each exchange) and acetone 3 times (6 h for each exchange) then degassed on ASAP 2420 for 10 h at 100 °C; SEM images were acquired using a Hitachi SU8030 scanning electron microscope. Prior to imaging, the sample was coated with OsO4 (~9 nm) in a Denton Desk III TSC Sputter Coater. CO_2, C_3H_8, and C_3H_6 sorption isotherms were measured on a Micromeritics 3Flex.

2. Micro electron diffraction crystallography.

Within the last twenty years, the use of electron diffraction to measure requisite diffraction data and intensities to model the solid-state structures of molecules and materials that crystallize in the sub-micron regime has become a topic of great interest to the chemical and structural biology communities. Now referred to as 3D ED (three-dimensional electron diffraction) or Micro ED (micro-electron diffraction), the stratagems by which these data are now collected closely mirror those utilized in X-ray diffraction, obviating the necessity that the user possess prior transmission electron microscope operational awareness. Until recently the capability of TEMs to collect electron diffraction data via the addition of various hardware supplements and software packages has been the sole avenue whereby this powerful analytical tool has been demonstrated to the scientific community. While this has yielded some promising results, the absence of a dedicated electron diffractometer that established a simple and easy-to-follow experimental workflow was not universally available and made it difficult for this technique to garner more expansive use as an analytical tool.

Modern dedicated electron diffractometers, such as the Rigaku XtaLAB Synergy-ED, have recently become available and offer a workflow paralleling that of modern X-ray diffractometers (*CrystEngComm*. **2021**, *23*, 8622). The XtaLAB Synergy-ED unifies the processes of sample screening, data collection and processing, and structure solution into a convenient, easy-to-follow process controlled through the well-known software package *CrysAlis*^{Pro}. The XtaLAB Synergy-ED was developed through collaborative efforts involving JEOL and Rigaku and relies on the former's expertise in microscopy in conjunction with the latter's experience in X-ray diffraction to provide a dedicated electron diffractometer capable of collecting high-quality data on both small molecule and protein samples (*Symmetry* **2023**, *15*, 1555).

The electron diffraction data were collected on multiple crystalline, nanometer size grains of Cu-ASY (data sets numbered 4463 to 4474) at room temperature using a XtaLAB Synergy-ED electron diffractometer equipped with a HyPix-ED detector optimized for operation in the electron diffraction experimental setup and a 200kV electron source at a wavelength of 0.025 Å. All measurements completed in less than ten minutes, resulting in a total experiment time of forty minutes. For improved data quality, a total of 6 measurements (4463, 4464, 4465, 4469, 4472, and 4474) were merged to build the final reflection file, resulting in an almost complete data set with a redundancy of 5.8. Data collection strategies for the individual grains and the merging of their respective datasets were completed using CrysAlis^{Pro} [CrysAlisPro, Rigaku Oxford Diffraction, version 171.43.44a, 2022]. Data processing was done using CrysAlis^{Pro} and included multi-scan absorption corrections applied using the SCALE3 ABSPACK scaling algorithm [SCALE3 ABSPACK–A Rigaku Oxford Diffraction program for Absorption Corrections, Rigaku Oxford Diffraction, 2017]. All structures were solved via intrinsic phasing methods using ShelXT [Sheldrick, G.M. (2015). Acta Cryst. A71, 3-8] and refined with ShelXL [Sheldrick, G.M. (2015). Acta Cryst. A71, 3-8] within the Olex2 graphical user interface [Dolomanov, O.V., Bourhis, L.J., Gildea, R.J, Howard, J.A.K. & Puschmann, H. (2009), J. Appl. Cryst. 42, 339-341]. The final structural refinement included anisotropic temperature factors on all constituent non-hydrogen atoms. Hydrogen atoms were attached via the riding model at calculated positions using suitable HFIX commands.

Table S1 shows the data collection details; Table S2 features the data quality statistics overview for all selected data collections; Table S3 gives the processing results for the merged data. Figure S0 presents the grain snapshots and diffraction images of all six data measurements.

Table S1. Data collection details for the six selected grains.

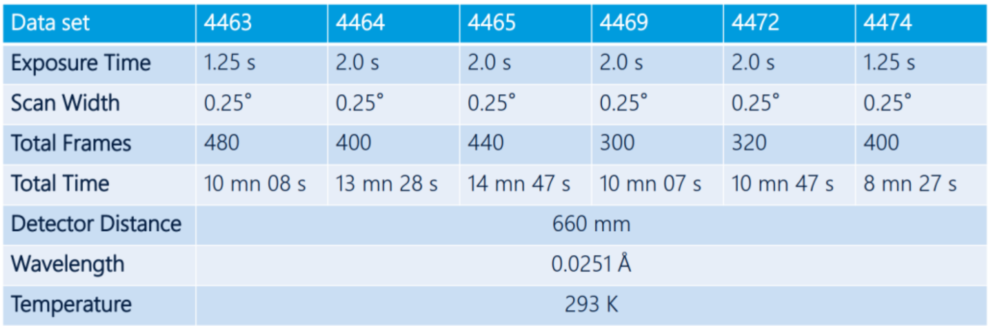

Data set	4463	4464	4465	4469	4472	4474
Exposure Time	1.25 s	2.0 s	2.0 s	2.0 s	2.0 s	1.25 s
Scan Width	0.25°	0.25°	0.25°	0.25°	0.25°	0.25°
Total Frames	480	400	440	300	320	400
Total Time	10 mn 08 s	13 mn 28 s	14 mn 47 s	10 mn 07 s	10 mn 47 s	8 mn 27 s
Detector Distance	660 mm					
Wavelength	0.0251 Å					
Temperature	293 K					

Table S2. Data quality statistics overview for the selected six data sets

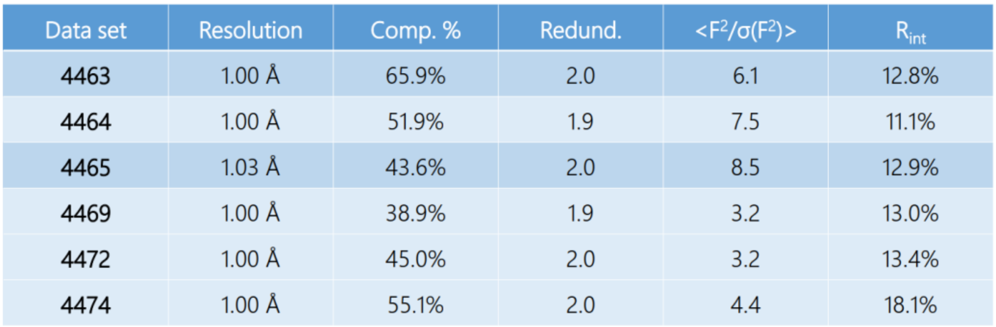

Data set	Resolution	Comp. %	Redund.	$\langle F^2/\sigma(F^2)\rangle$	R_{int}
4463	1.00 Å	65.9%	2.0	6.1	12.8%
4464	1.00 Å	51.9%	1.9	7.5	11.1%
4465	1.03 Å	43.6%	2.0	8.5	12.9%
4469	1.00 Å	38.9%	1.9	3.2	13.0%
4472	1.00 Å	45.0%	2.0	3.2	13.4%
4474	1.00 Å	55.1%	2.0	4.4	18.1%

Table S3. Processing results for the merged data.

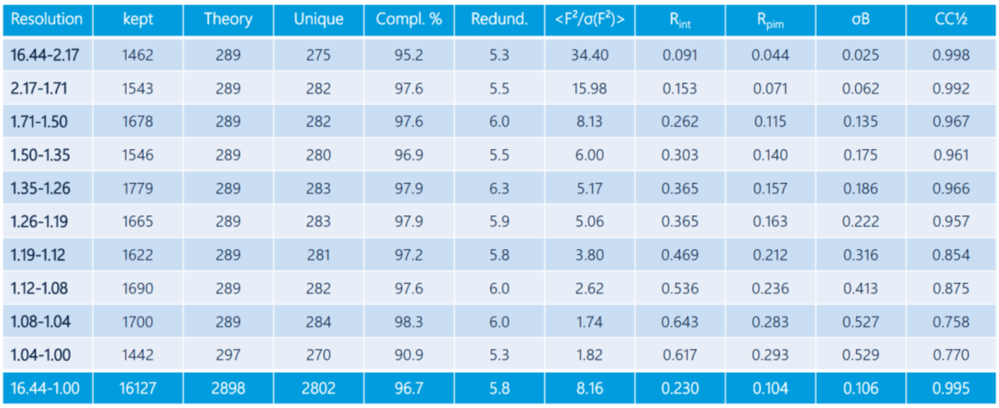

Resolution	kept	Theory	Unique	Compl. %	Redund.	$\langle F^2/\sigma(F^2)\rangle$	R_{int}	R_{pim}	σB	CC½
16.44-2.17	1462	289	275	95.2	5.3	34.40	0.091	0.044	0.025	0.998
2.17-1.71	1543	289	282	97.6	5.5	15.98	0.153	0.071	0.062	0.992
1.71-1.50	1678	289	282	97.6	6.0	8.13	0.262	0.115	0.135	0.967
1.50-1.35	1546	289	280	96.9	5.5	6.00	0.303	0.140	0.175	0.961
1.35-1.26	1779	289	283	97.9	6.3	5.17	0.365	0.157	0.186	0.966
1.26-1.19	1665	289	283	97.9	5.9	5.06	0.365	0.163	0.222	0.957
1.19-1.12	1622	289	281	97.2	5.8	3.80	0.469	0.212	0.316	0.854
1.12-1.08	1690	289	282	97.6	6.0	2.62	0.536	0.236	0.413	0.875
1.08-1.04	1700	289	284	98.3	6.0	1.74	0.643	0.283	0.527	0.758
1.04-1.00	1442	297	270	90.9	5.3	1.82	0.617	0.293	0.529	0.770
16.44-1.00	16127	2898	2802	96.7	5.8	8.16	0.230	0.104	0.106	0.995

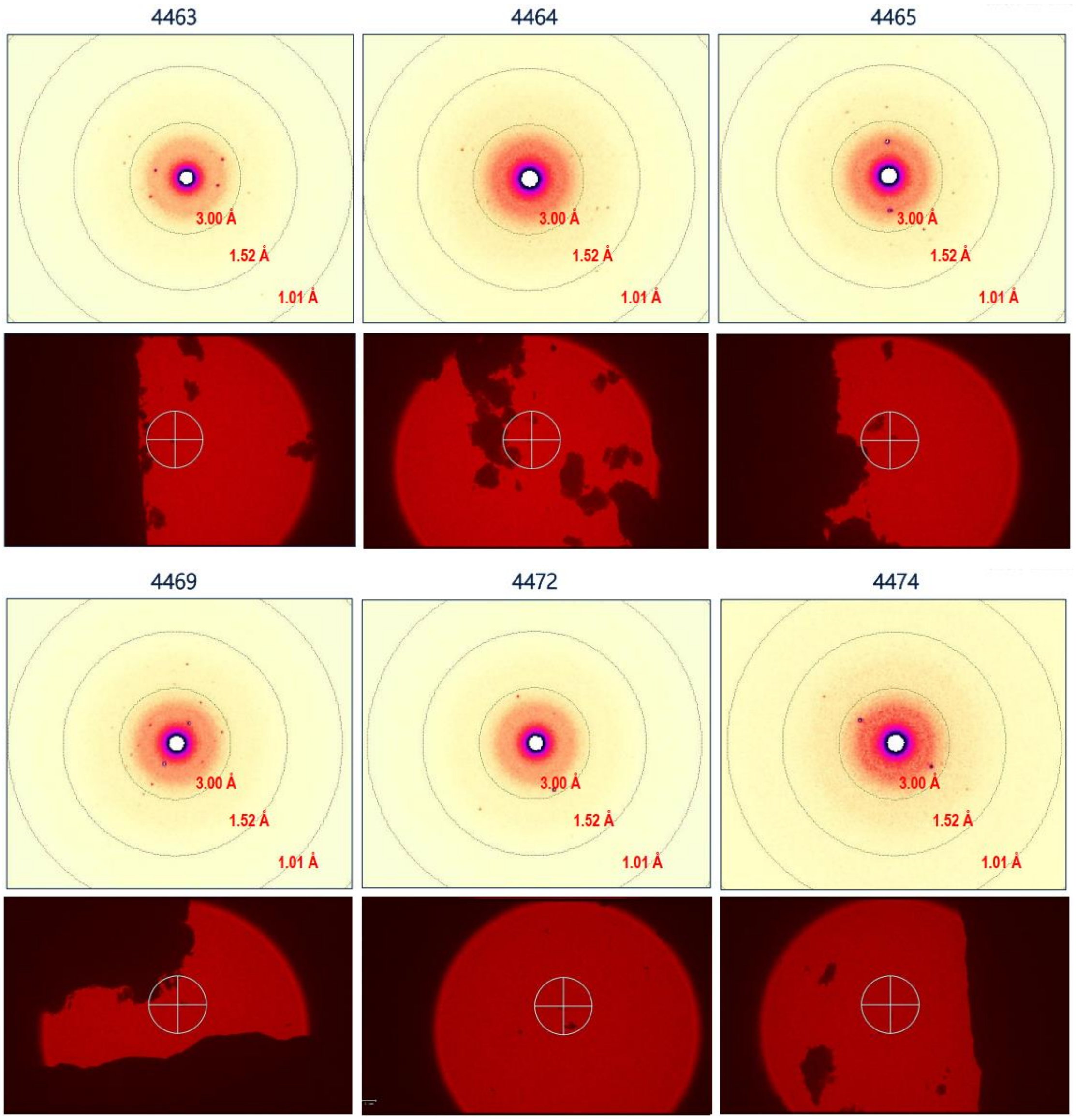

Figure S0. Grain snapshots and diffraction images of the six data sets.

Crystal data and details of the data collection are given in **Tables S4**. CCDC 2269110 contains the supplementary crystallographic data for this paper. The data can be obtained free of charge from The Cambridge Crystallographic Data Centre via www.ccdc.cam.ac.uk/data_request/cif. The relatively high R_1 and

wR_2 values and ADP alerts are due to the poor crystal data collected by ED technique at room temperature, and these poor parameters are commonly observed in other reported crystal data sets (*Nat. Commun*. **2022**, *13*, 415 / *CrystEngComm*. **2021**, *23*, 8622).

Table S4. **Crystal data and structure refinements**

Identification Code	Cu-ASY
Empirical formula	$C_{27} H_{16} Cu_2 O_7$
Formula weight	579.5
Temperature (K)	293(2) K
Crystal system	Triclinic
Space group	*P-1*
Unit cell dimensions	a = 5.528(2) Å α = 77.15(3) b = 15.184(6) Å β = 83.49(4) c = 16.951(7) Å γ = 86.91(4)
Volume (Å^3), Z	1377.7(10), 2
Density	1.395
F(000)	199
Reflections	16127 / 2802
Completeness to	0.719 / 96.7 %
R_{int}	0.2515

Refinement	Full-matrix least-squares on *F*^2
Data / restraints /	2802 / 854 / 218
Goodness-of-fit on	1.247
Final *R* indices	R_1 = 0.2869, wR_2 = 0.6678
R indices (all data)	R_1 = 0.3683, wR_2 = 0.7456
Largest diff. peak	0.374 / -0.356

3. Fitting of pure component isotherms

The experimentally collected isotherms for C_3H_8 and C_3H_6 at 273 K, 298, and 313 K in Cu-ASY were fitted with the dual-site Langmuir-Freundlich equation.

$$q = q_{A,sat}\frac{b_A p^{c_A}}{1 + b_A p^{c_A}} + q_{B,sat}\frac{b_B p^{c_B}}{1 + b_B p^{c_B}}$$

The Langmuir parameters for each site is temperature-dependent,

$$b_A = b_{A0} exp\left(\frac{E_A}{RT}\right); b_B = b_{B0} exp\left(\frac{E_B}{RT}\right)$$

where *p* (unit: kPa) is the pressure of the bulk gas at equilibrium with the adsorbed phase, *q* (unit: mmol g^{-1}) is the adsorbed amount per mass of adsorbent, q_{sat} (unit: mmol/g) is the saturation capacities, *c* (unit: kPa^{-1}) is the affinity coefficient.

Calculation of isosteric heat of adsorption (Q_{st})

The Clausius-Clapeyron equation was employed to calculate the heat of adsorption:

$$Q_{st} = RT^2\left(\frac{\partial ln\, p}{\partial T}\right)_q$$

was determined using the pure component isotherm fits using the Virial equation.

IAST calculations of adsorption selectivity

For the separation of a binary mixture of components C_3H_8 and C_3H_6, the adsorption selectivity is defined by

$$S_{ads} = \frac{q_1/q_2}{y_1/y_2}$$

In equation (4), the q_1, and q_2 represent the molar loadings of C_3H_8 and C_3H_6, expressed in mol kg^{-1}, within the MOF that is in equilibrium with a bulk fluid mixture with mole fractions y_1, and $y_2 = 1-y_1$. The molar loadings, also called gravimetric uptake capacities, are usually expressed with the units mol kg^{-1}. The IAST calculations of 50/50 mixture adsorption taking the mole fractions $y_1 = 0.5$ and $y_2 = 1-y_1 = 0.5$ for a range of pressures up to 101 kPa and 298 K were performed.

Breakthrough experiments

The breakthrough experiments were carried out in a dynamic gas breakthrough setup. A stainless-steel column with inner dimensions of 4 mm and a length of 80 mm was used for sample packing. Microcrystalline samples (0.42 g of Cu-ASY microcrystals) were air dried and then packed into the columns. The columns were activated in vacuum oven at 80°C. The mixed gas flow of binary gas (C_3H_6/C_3H_8 at 50/50, v/v) and pressure were controlled by using a pressure controller valve and a mass flow controller. Outlet effluent from the column was continuously monitored using gas chromatography (GC-2014, Shimadzu) with a thermal conductivity detector. The column packed with activated sample was first purged with helium gas flow for 1 h at room temperature. The mixed gas flow rate during the breakthrough process is 2 mL min^{-1} at 1 bar. After the breakthrough experiment, the sample was purged with helium gas flow (40 mL min^{-1}) at 298 K, from which the outlet effluent was monitored. The column can be regenerated and purged with helium gas flow (50 mL min^{-1}) at 298 K for 20 min before next cycle.

Since Cu-ASY is a C_3H_8 selective material, the productivity of C_3H_6 can be directed calculated based on the breakthrough time obtained from the breakthrough experiment. The breakthrough time of C_3H_6 is 2.2 min/g, the gas flow of C_3H_6 is 1.0 cm^3/min, therefore the C_3H_6 productivity is calculated to be 2.2 min/g * 1 cm^3/min = 2.2 cm^3/g or 2.2 L/kg.

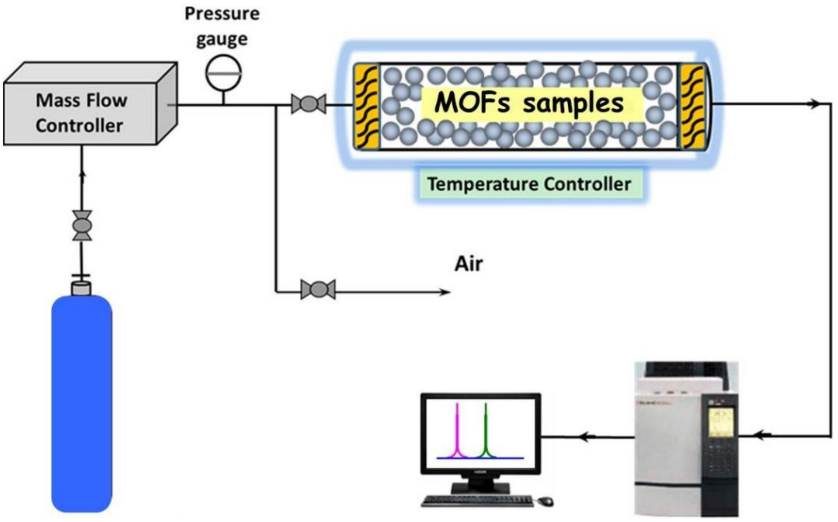

4. Calculation details.

All the calculations were performed in the Material Studio 2019 package (BIOVIA, Dassault Systems, Materials Studio 2019, Dassault Systems, San Diego, 2018). The crystal structure of Cu-ASY was taken as initial geometry for further computational calculations. The partial charge of framework atoms was taken from Mulliken charge and considered as rigid in the simulations. The charges of gas molecules were derived from ESP charge. The binding sites of propylene and propane were first investigated by GCMC-simulated annealing calculations performed for one molecule within a unit cell, which started from an initial temperature of 1×10^5 K, followed by 1.0×10^6 Monte Carlo steps. Universal forcefield (UFF) was used, in which the interaction energy between gas molecules and frameworks were computed through the Coulomb and Lennard-Jones 6-12 (LJ) potentials. The cut-off radius was chosen as 12 Å for the LJ potential and the long-range electrostatic interactions were handled by the Ewald summation method, with a Buffer width of 0.5 Å and accuracy of 1×10^{-5} kcal mol^{-1}. The equilibration steps and the production steps were set as 1×10^6 and 1×10^7, respectively. The preliminary host-guest structure was further allowed to fully relaxed and optimized using first-principle density functional theory (DFT) in the CASTEP code

(Kristallogr., 2005, 220, 567.) The generalized gradient approximation (GGA) with the Perdew-Burke-Ernzerhof (PBE) functional (Phys. Rev. Lett. 1996, 77, 3865) and on-the-fly generated ultrasoft pseudopotentials[3] were used. Grimme (G06) semi-empirical methods to describe the long-range van der Waals interactions. A cutoff energy of 650 eV and a 2 × 2 × 2 *k*-point mesh was found to be enough for the total energy to converge within 1×10^{-5} eV atom $^{-1}$. Full geometry optimizations were performed on the structures loaded with one C_3H_6 or C_3H_8 molecule. The static binding energy was calculated: $\Delta E = E(\text{MOF}) + E(\text{gas}) - E(\text{MOF} + \text{gas})$.

5. Synthesis of organic linkers.

The two C_{2v} symmetric tritopic linkers were synthesized according to the reported procedures (*J. Am. Chem. Soc.* 2007, *129*, 15740 / *J. Am. Chem. Soc.* 2010, *132*, 13941). The C_s symmetric tritopic linker (H_3**L**) was synthesized according to the reported procedures (*Chem. Eur. J.* 2015, *21*, 5954) and the synthetic scheme was shown below.

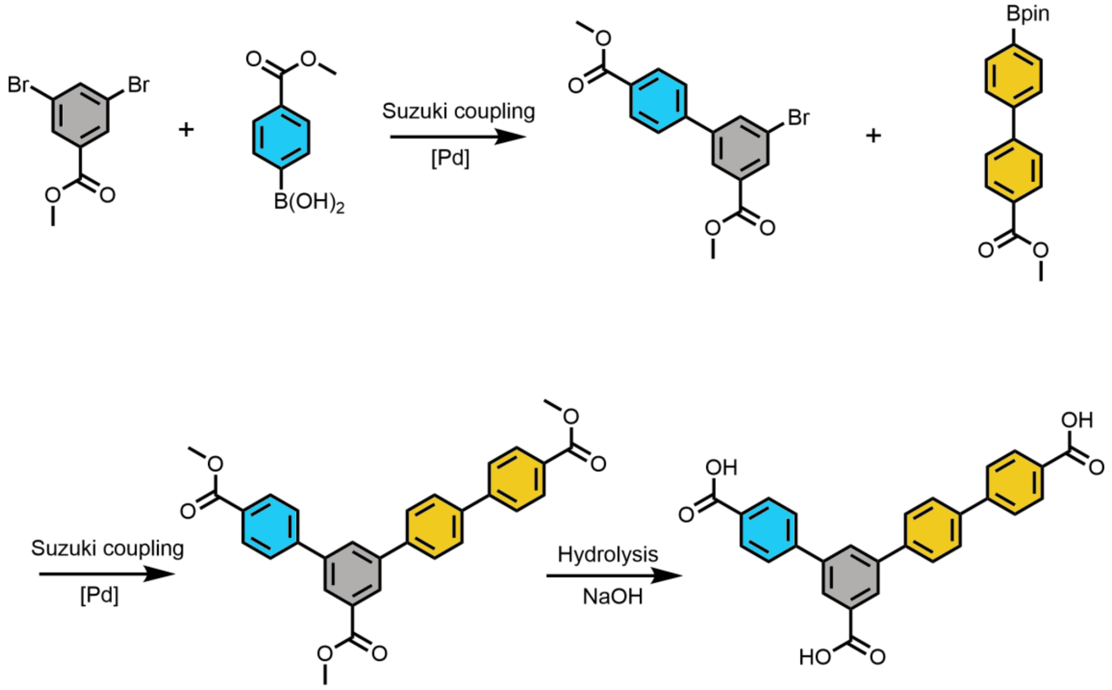

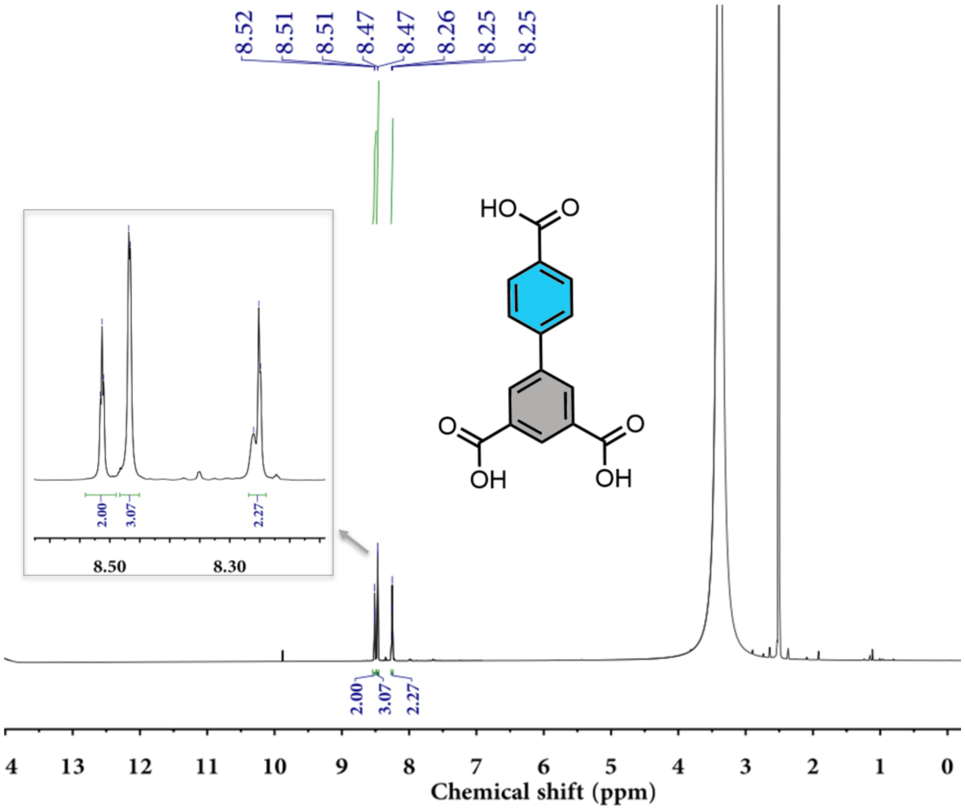
8.52
8.51
8.51
8.47
8.47
8.26
8.25
8.25
HO
O
O
OH
O
OH
2.00
3.07
2.27
8.50
8.30
2.00
3.07
2.27
4
13
12
11
10
9
8
7
6
5
4
3
2
1
0
Chemical shift (ppm)

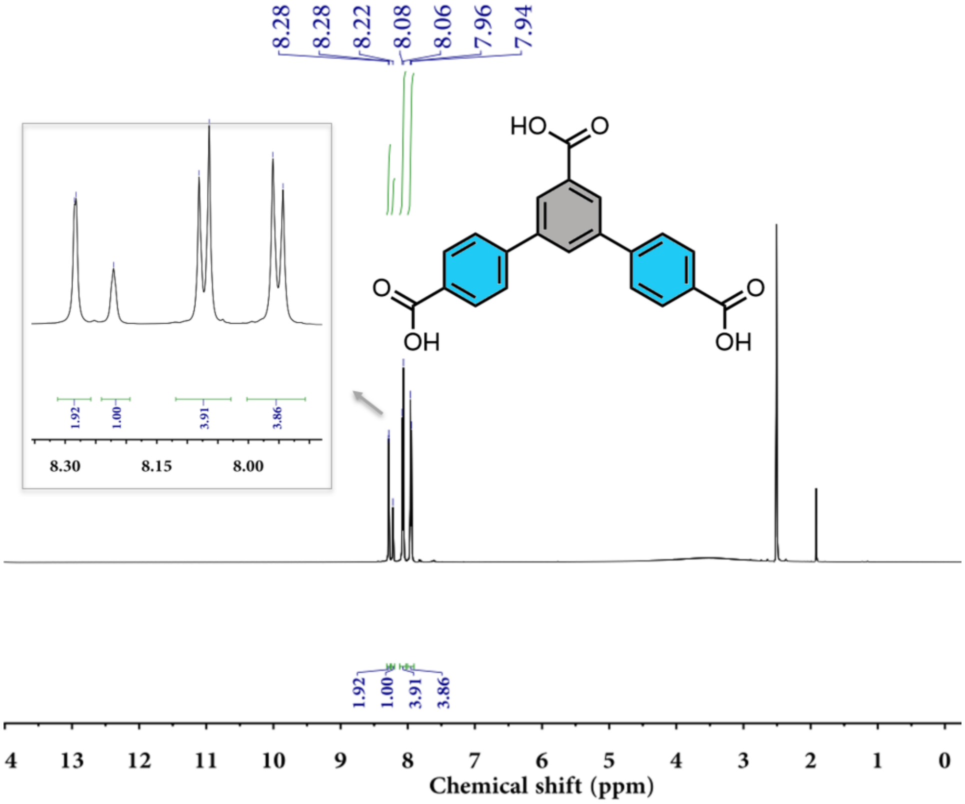
8.28
8.28
8.22
8.08
8.06
7.96
7.94
HO
O
O
OH
O
OH
1.92
1.00
3.91
3.86
8.30
8.15
8.00
1.92
1.00
3.91
3.86
4
13
12
11
10
9
8
7
6
5
4
3
2
1
0
Chemical shift (ppm)

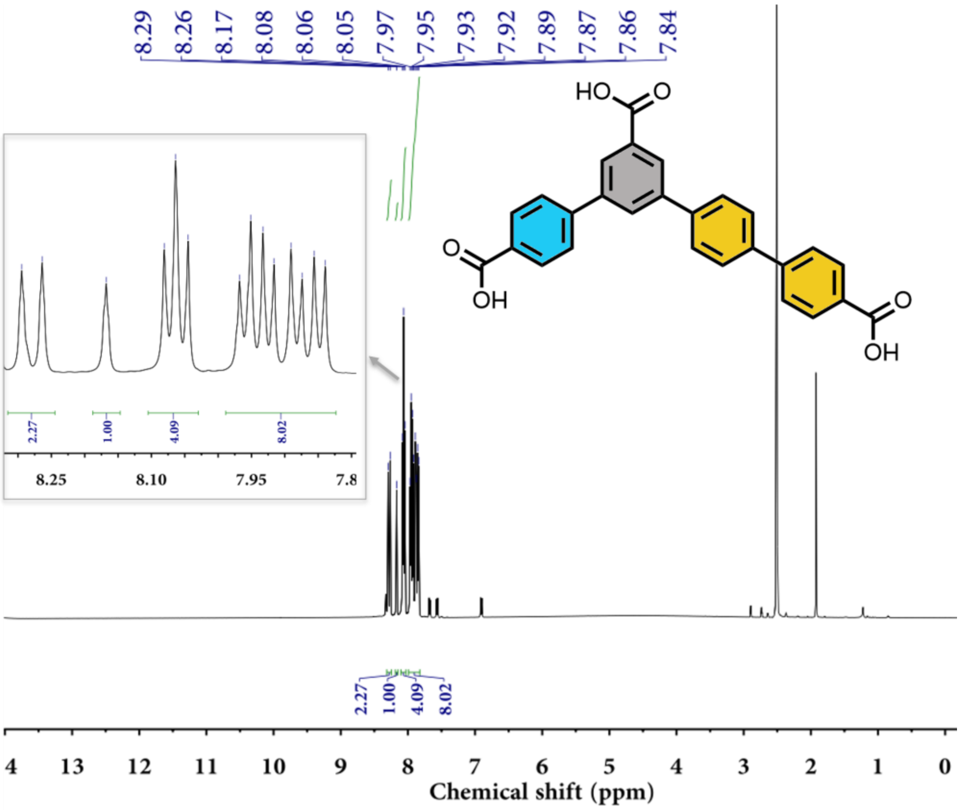
8.29
8.26
8.17
8.08
8.06
8.05
7.97
7.95
7.93
7.92
7.89
7.87
7.86
7.84
HO
O
O
OH
O
OH
2.27
1.00
4.09
8.02
8.25
8.10
7.95
7.8
2.27
1.00
4.09
8.02
4
13
12
11
10
9
8
7
6
5
4
3
2
1
0
Chemical shift (ppm)

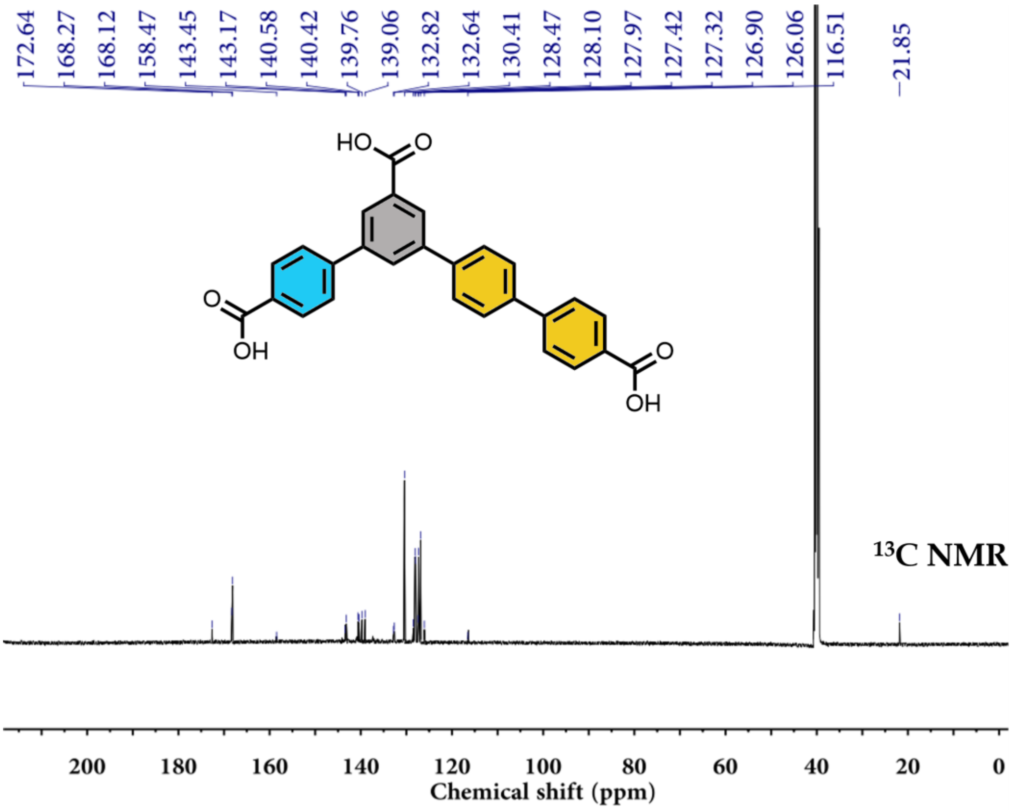
172.64
168.27
168.12
158.47
143.45
143.17
140.58
140.42
139.76
139.06
132.82
132.64
130.41
128.47
128.10
127.97
127.42
127.32
126.90
126.06
116.51
−21.85
HO
O
O
OH
O
OH
^{13}C NMR
200
180
160
140
120
100
80
60
40
20
0
Chemical shift (ppm)

6. Synthesis of Cu-MOFs.

UMCM-150: 100 mg $Cu(NO_3)_2 \cdot 3H_2O$ and 50 mg biphenyl-3,4′,5-tricarboxylate were added into a mixture of DMF/dioxane/H_2O (4 mL/1 mL/1 mL) in a 2-dram vial. The solution was sonicated for 5 minutes and then placed into an 80 ℃ oven for 2 days. Large blue hexagonal crystals were collected for further characterizations and measurements.

UMCM-151: 100 mg $Cu(NO_3)_2 \cdot 3H_2O$ and 50 mg 3,5-di(4'-carboxylphenyl)benozoic acid were added into a mixture of DMF/dioxane/H_2O (4 mL/1 mL/1 mL) in a 2-dram vial. The solution was sonicated for 5 minutes and then placed into an 80 ℃ oven for 2 days. Large blue block crystals were collected for further characterizations and measurements.

Cu-ASY: 100 mg $Cu(NO_3)_2 \cdot 3H_2O$ and 50 mg H_3**L** were added into a mixture of DMF/dioxane/H_2O (4 mL/1 mL/1 mL) in a 2-dram vial. The solution was sonicated for 5 minutes and then placed into an 80 ℃ oven for 2 days. Blue powders were collected for further characterizations and measurements.

7. Figures S1-S3. Additional X-ray crystallographic structures

There is a strategy to assess the unicity of a net. Following the rules described in the CG&D paper "Deconstruction of Crystalline Networks into Underlying Nets: Relevance for Terminology Guidelines and Crystallographic Databases" *Cryst. Growth Des.*, **2018**, *18*, 3411. It is possible to analyze any structure with at least 2 representations: (1) Standard = the nodes are the single point metals and the other nodes are what remain i.e. single atoms like oxygens or multi branched ligands. This representation is always possible and is very useful for data base retrieval of isoreticular compounds; (2) Cluster all or single node: this representation is tricky for rod-MOF because the cluster algorithm will find an infinite SBU, so the researchers need to decide how to simplify/describe such infinite SBU. The modes are with the Point-of-Extension (PE) introduced by Mike O'Keeffe in ref 15 , and as PE&M or STR as in ref 45 in the main text.

The ToposPro team developed a database of standard description of MOF as they are reported in CSD, and updated every year. The database is Topcryst: https://topcryst.com/ (see the open access ref: https://doi.org/10.1080/27660400.2022.2088041). So, we can search our MOF by the standard underlying nets, and we found only two structures (refcode: FAHNOT and KUZBAL) that are chemically very different from ours, not rod-MOF but containing SBU dimeric Cu_2 and Zn_2. So, we are confident that our rod-MOF is unique.

About the 4^4(3,3) *qbe* tubule, it has been observed only in three metal-organic nanotubes (*Inorg. Chem. Commun.* **2008**, *11*, 616 with refcode of AFOGAE), (*Inorg. Chem.* **2015**, *54*, 6680 with refcode of BUGXIM), and (*Angew. Chem., Int. Ed.* **2009**, *48*, 9461 with refcodes of SUKNOC and SUKPAQ), and never been reported in MOFs to date.

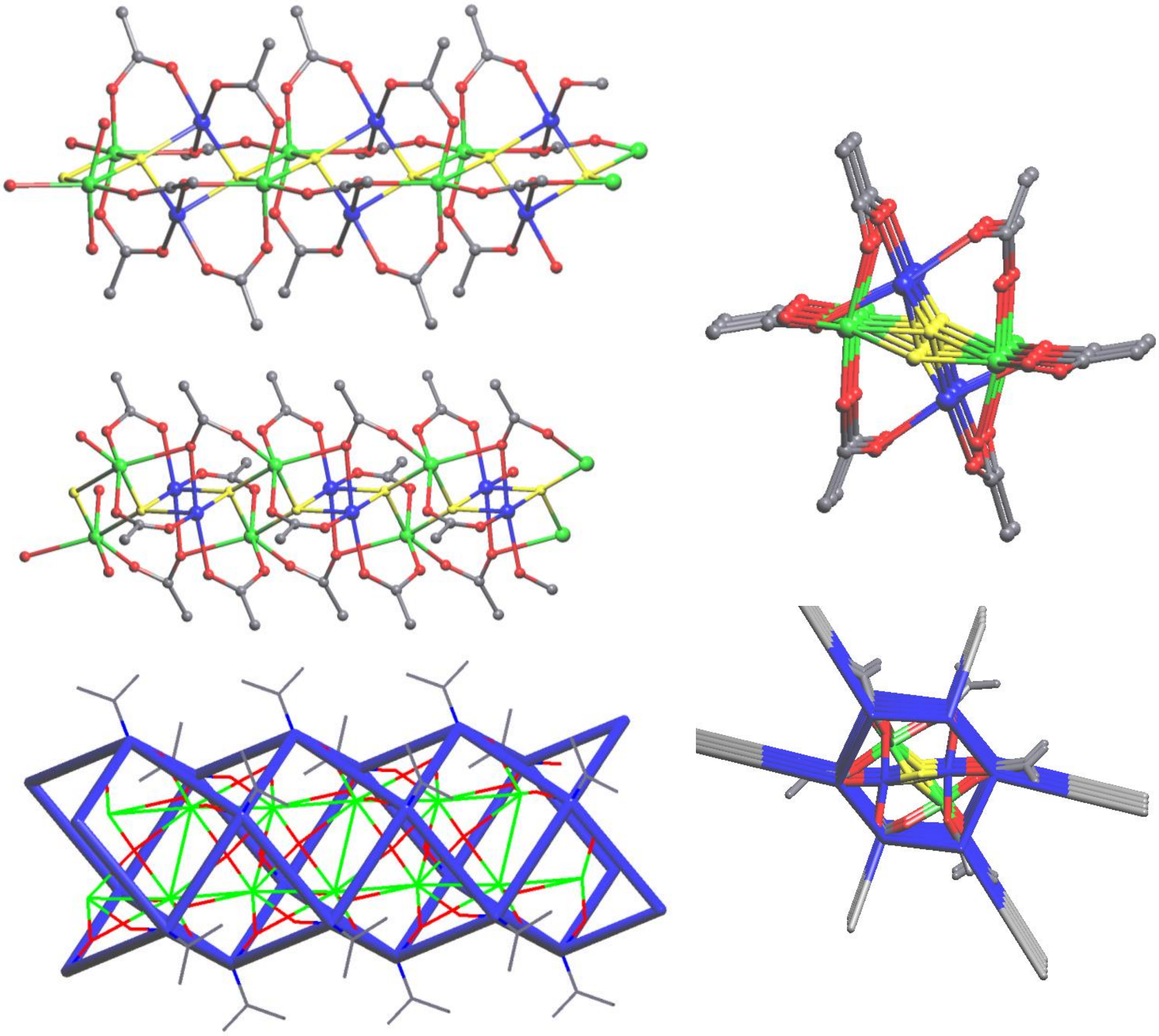

Figure S1. The rod SBU with Cu square pyramidal in blue, Cu octahedral in green and the O of the OH group in yellow. There are three distinct carboxylate, two μ^2 and one μ^3. Bottom some views of the tube SBU **qbe** / 4^4(3,3) in blue obtained following the PE (point-of-extension) rules that join the C atoms of the carboxylate from the ligands.

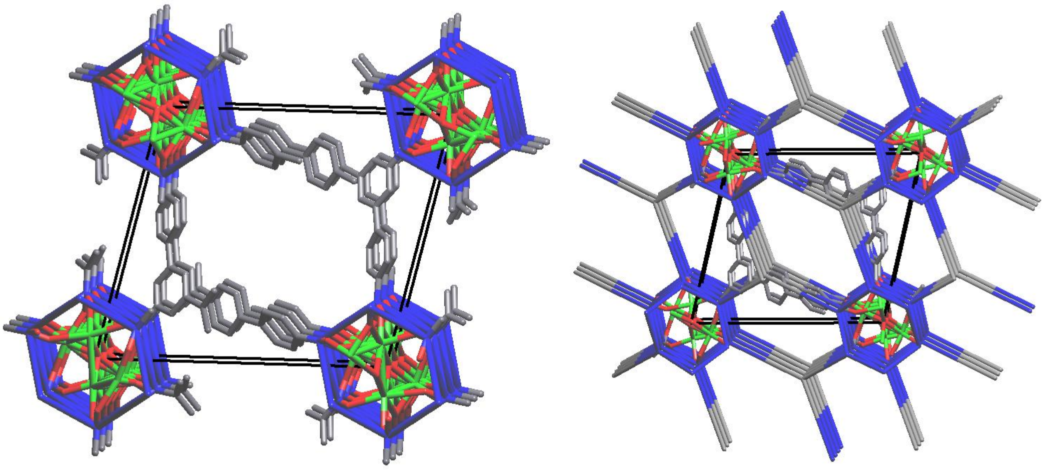

Figure S2. Views of the underlying nets together with the crystal structure, left: the SBU **qbe** / $4^4(3,3)$ and right: the 3,5-c **gfc** net.

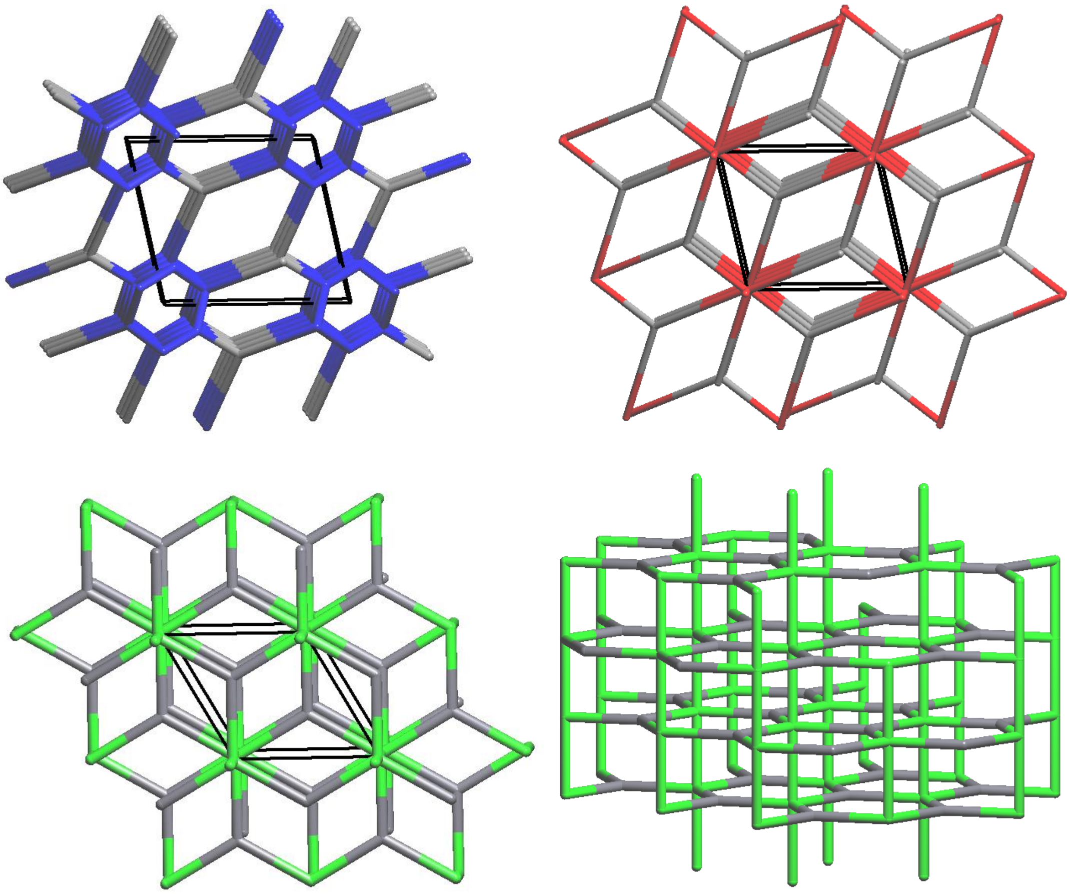

Figure S3. (Top) two alternative description of the underlying net from the crystal structure: left the 3,5-c **gfc** (PE description) right 3,5-c **gra** (STR description). (Bottom) The ideal **gra** net showing the ABAB stacking of **hcb** graphene like layers

8. Figures S4-S6. Additional PXRD patterns

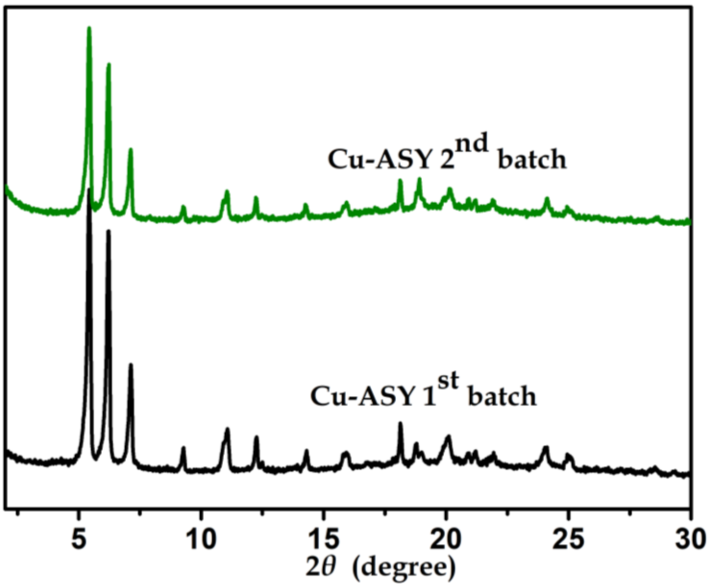

Figure S4. PXRD patterns of Cu-ASY synthesized in different batches, showing the consistence of phase purity.

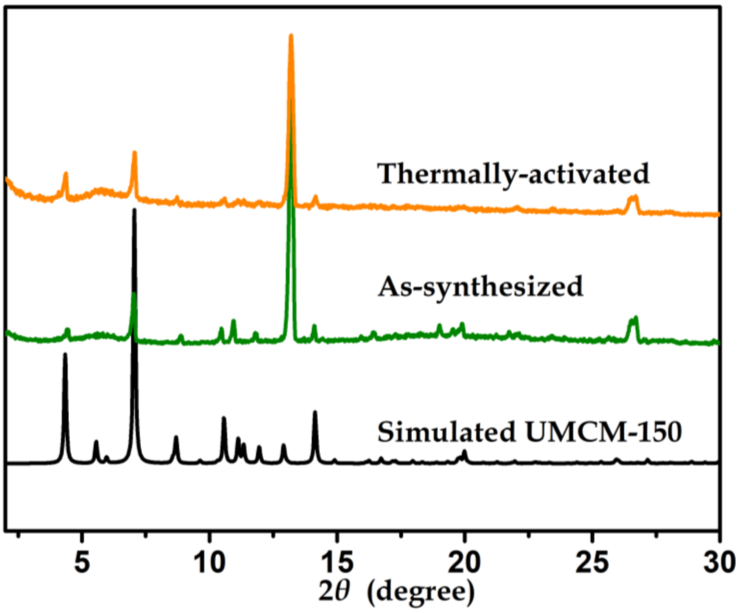

Figure S5. PXRD patterns of UMCM-150, showing its bulk phase purity. The difference of peak intensities at about 4, 7, and 13.5 degrees are the result of preferred orientation effect coming from the very thin crystal morphology.

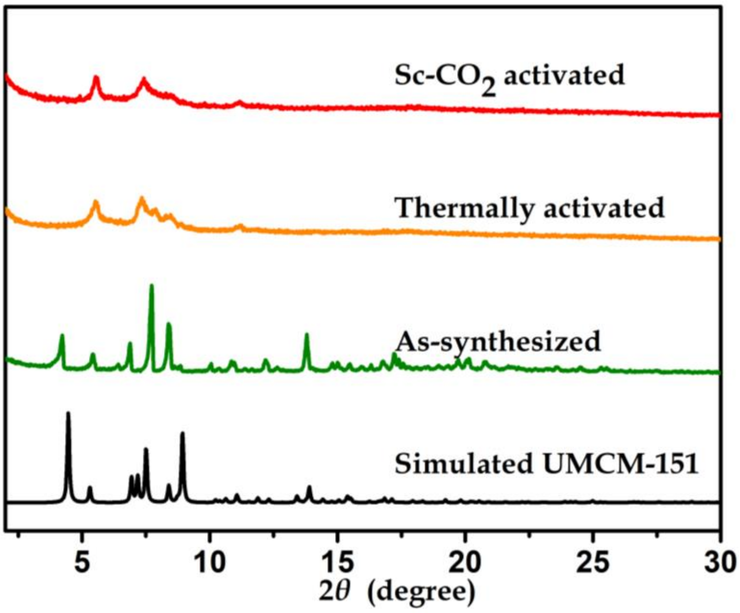

Figure S6. PXRD patterns of UMCM-151, showing its bulk phase purity and partial structural collapse upon activation.

9. Figure S7-S10. Additional CO_2 and N_2 sorption isotherms

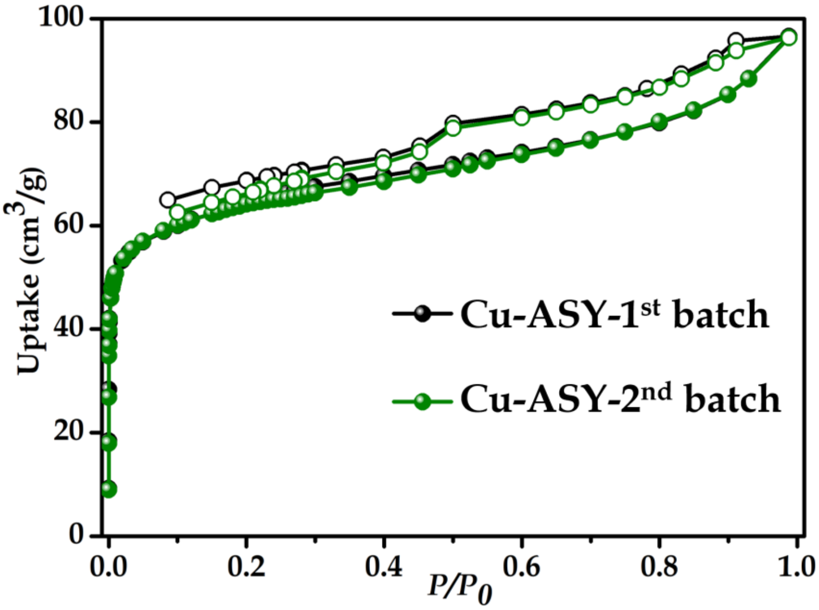

Figure S7. N_2 sorption isotherms of Cu-ASY synthesized in different batches.

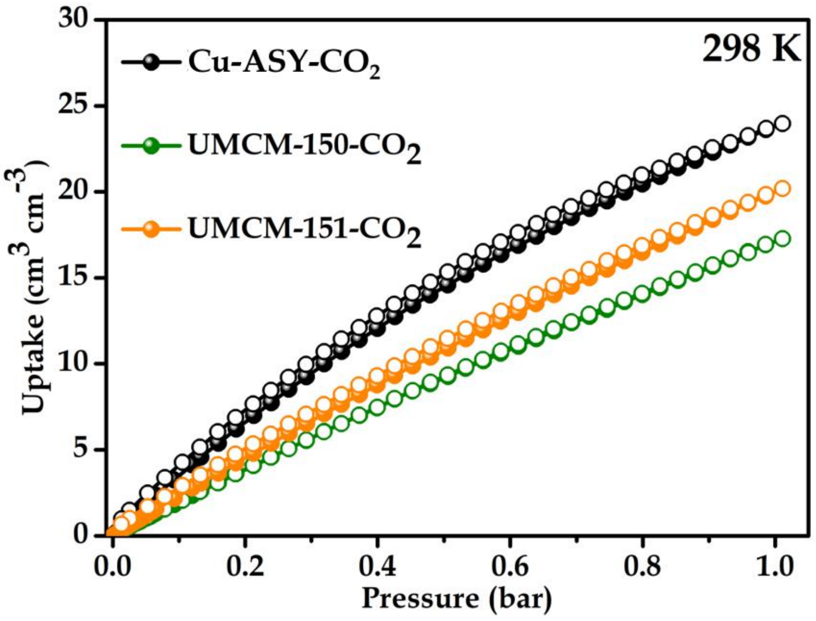

Figure S8. CO_2 sorption isotherms of Cu-ASY, UMCM-150, and UMCM-151 at room temperature and ambient pressure.

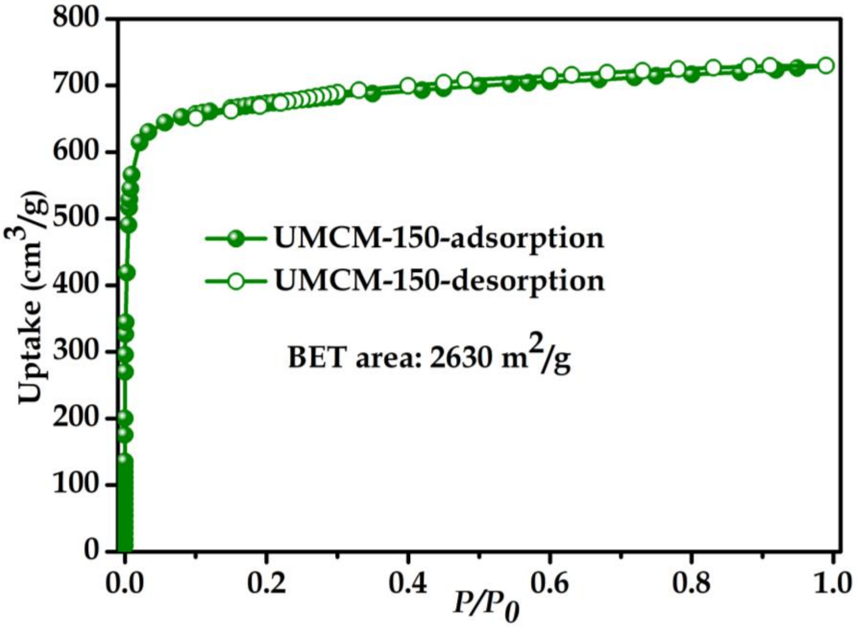

Figure S9. N_2 sorption isotherms of UMCM-150.

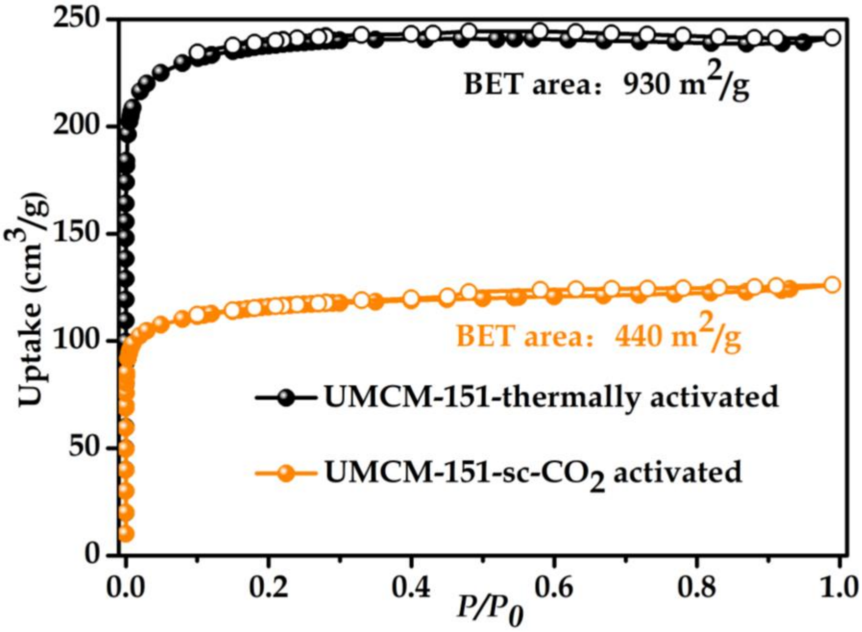

Figure S10. N_2 sorption isotherms of UMCM-151.

10. Figure S11-24. Additional C_3H_8/C_3H_6 sorption isotherms

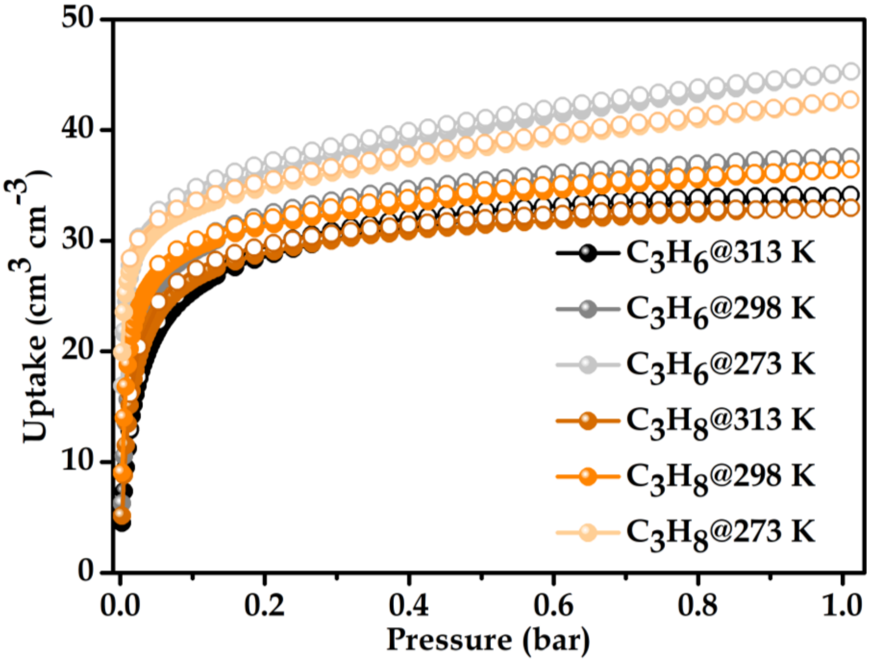

Figure S11. C_3H_6 and C_3H_8 adsorption/desorption isotherms of Cu-ASY at different temperatures.

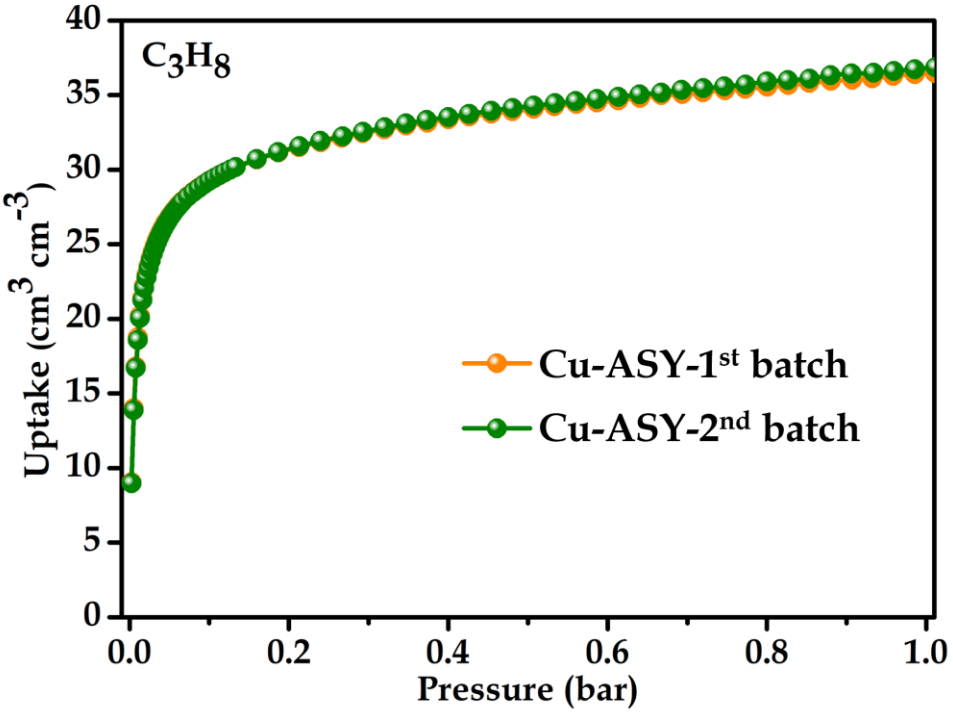

Figure S12. C_3H_8 adsorption isotherms of Cu-ASY synthesized in different batches.

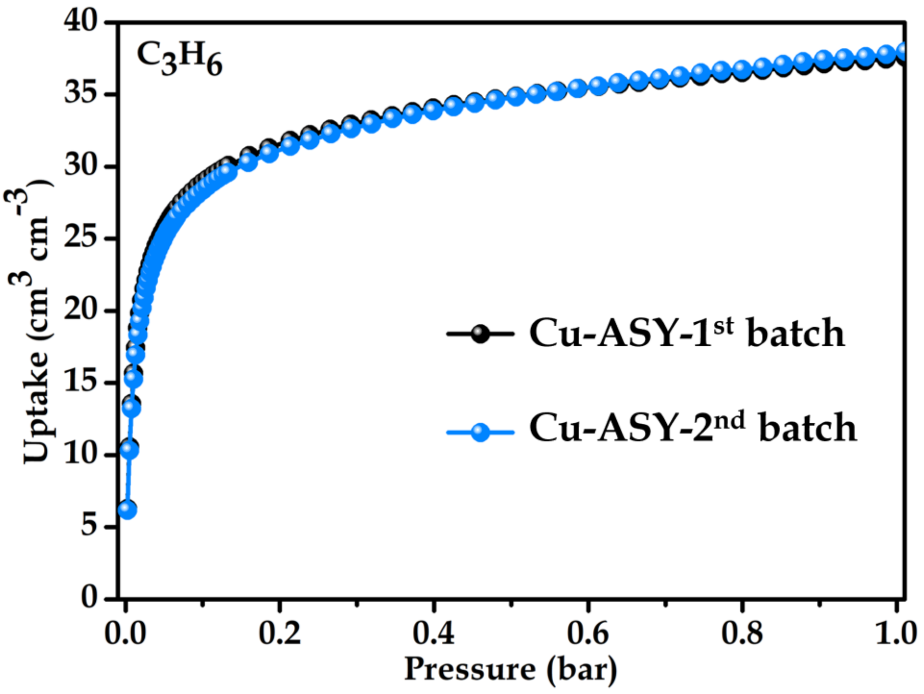

Figure S13. C_3H_6 adsorption isotherms of Cu-ASY synthesized in different batches.

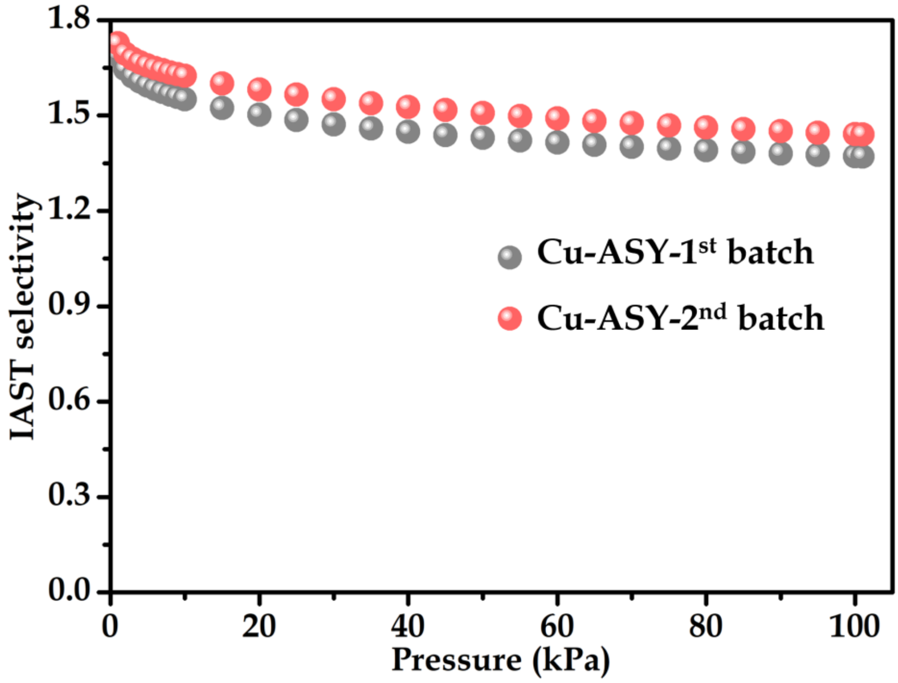

Figure S14. IAST selectivity calculations of Cu-ASY samples synthesized in different batches.

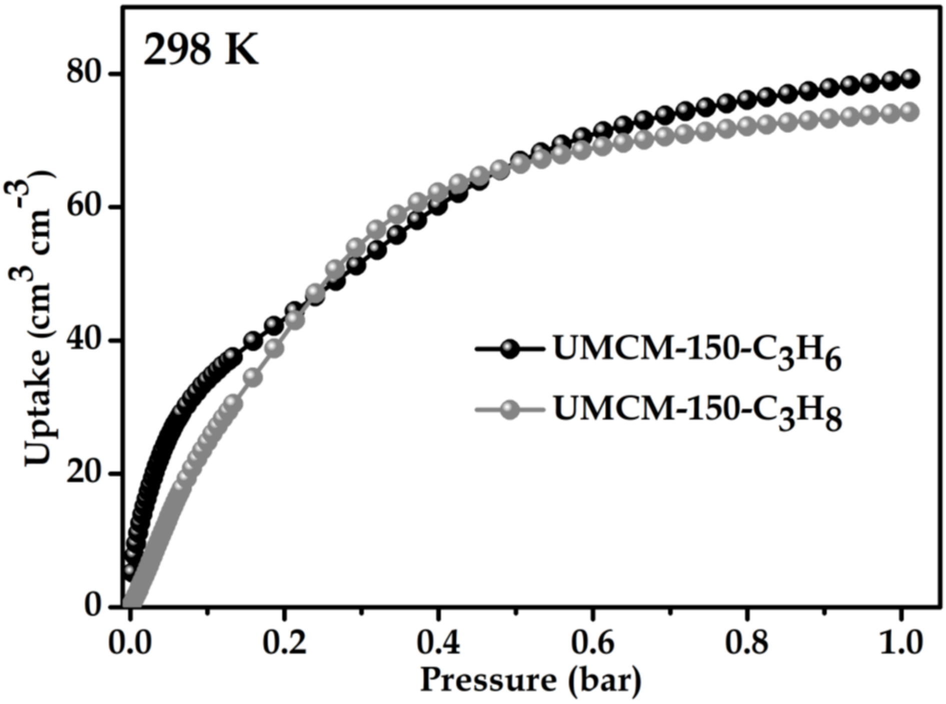

Figure S15. C_3H_6 and C_3H_8 sorption isotherms collected at 298 K and 1 bar of UMCM-150.

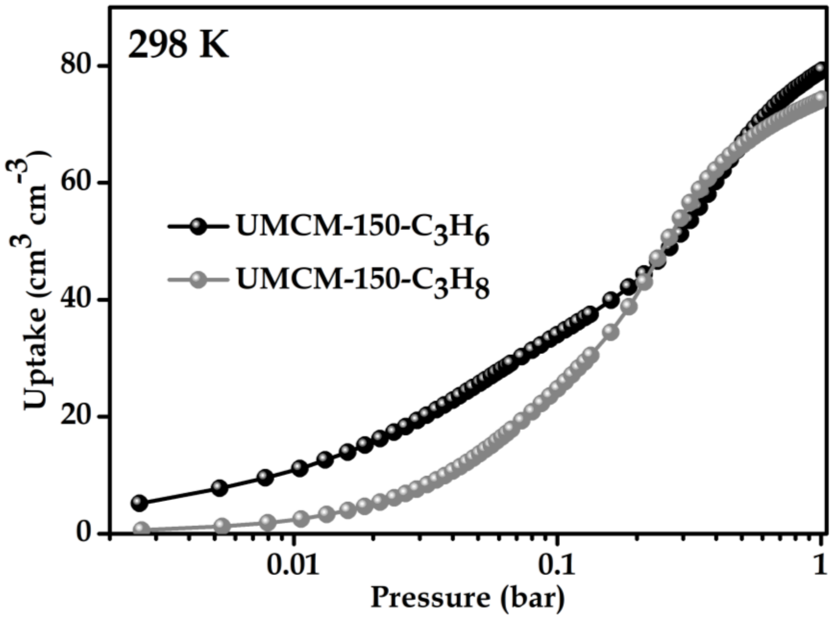

Figure S16. Enlarged C_3H_6 and C_3H_8 sorption isotherms of UMCM-150.

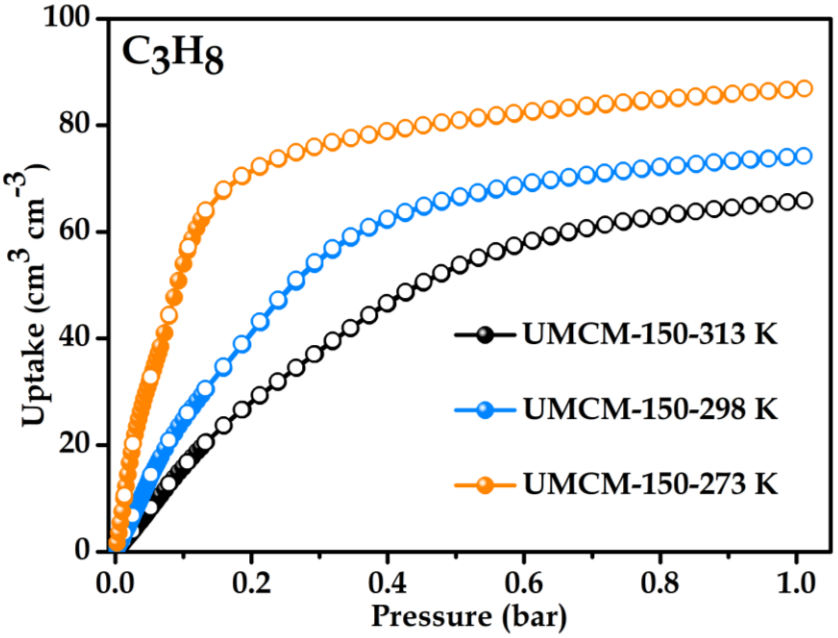

Figure S17. C_3H_8 sorption isotherms of UMCM-150 at different temperatures.

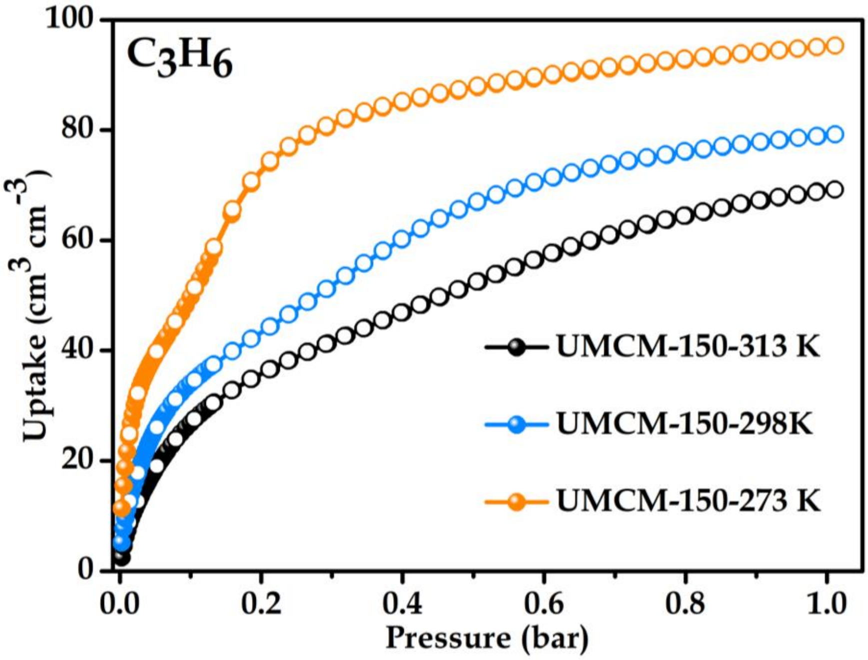

Figure S18. C_3H_6 sorption isotherms of UMCM-150 at different temperatures.

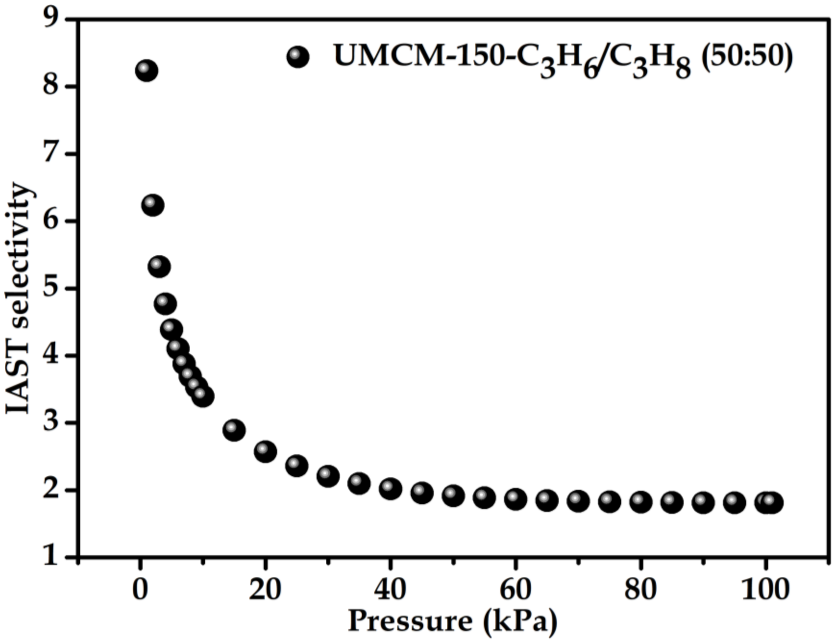

Figure S19. IAST selectivity of UMCM-150 for equivalent C_3H_6/C_3H_8 gas mixture.

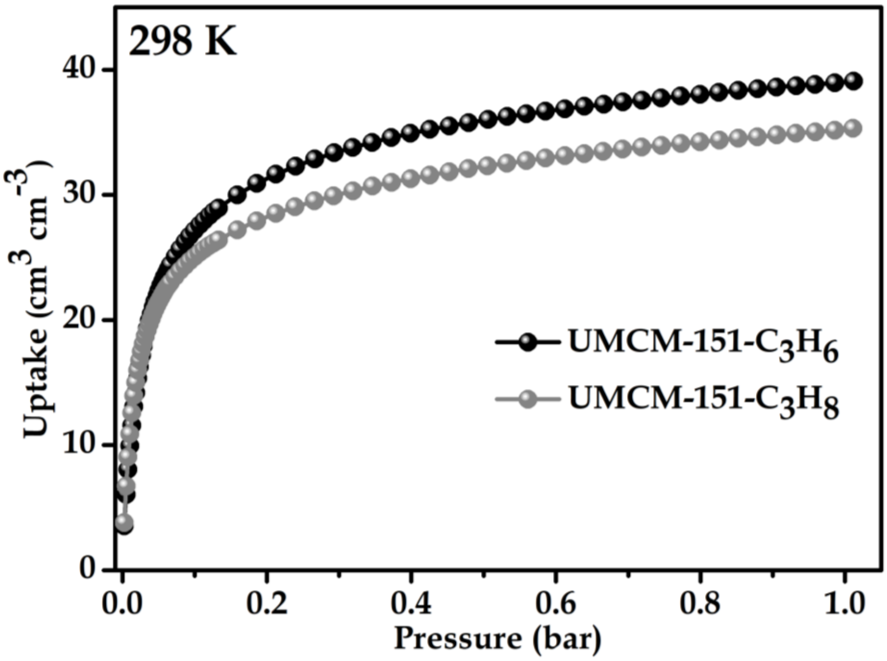

Figure S20. C_3H_6 and C_3H_8 sorption isotherms collected at 298 K and 1 bar of UMCM-151.

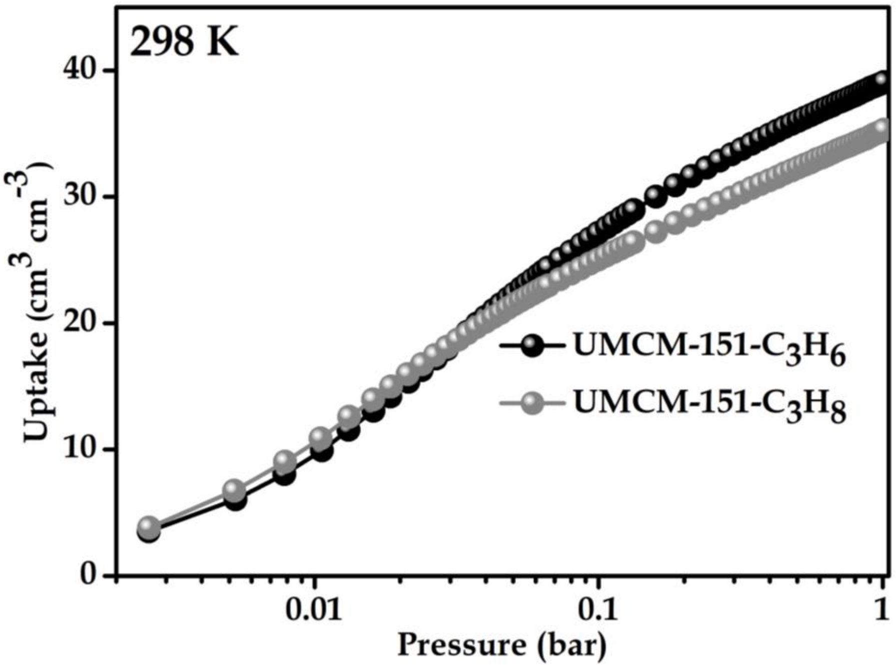

Figure S21. Enlarged C_3H_6 and C_3H_8 sorption isotherms of UMCM-151.

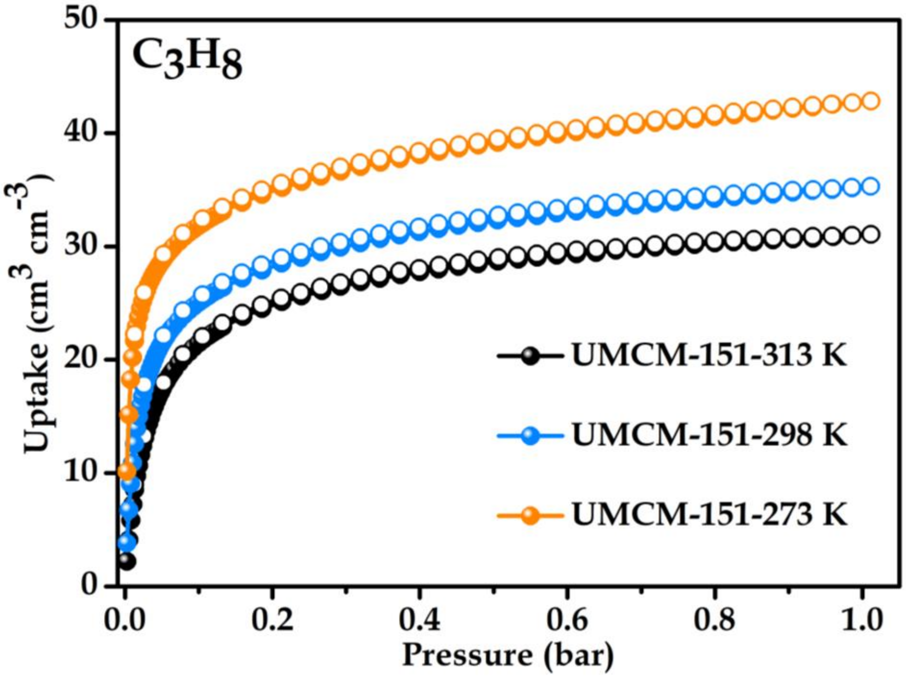

Figure S22. C_3H_8 sorption isotherms of UMCM-151 at different temperatures.

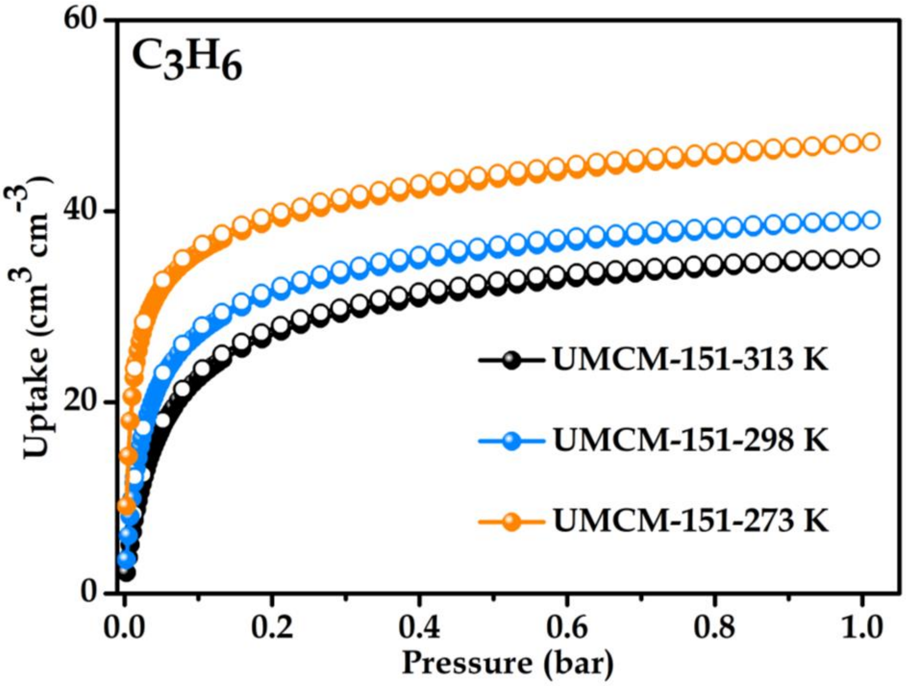

Figure S23. C_3H_6 sorption isotherms of UMCM-151 at different temperatures.

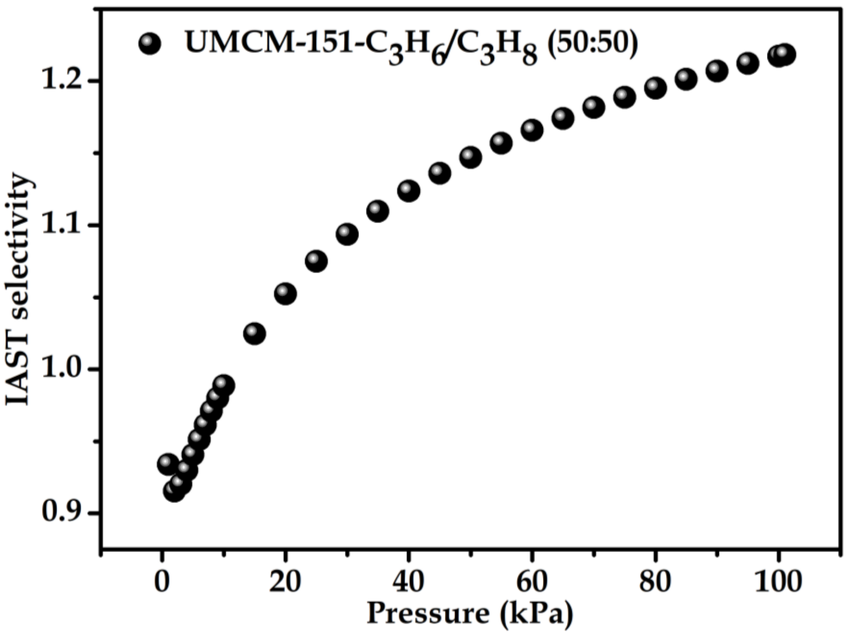

Figure S24. IAST selectivity of UMCM-151 for equivalent C_3H_6/C_3H_8 gas mixture.

11. Figure S25. TGA curves

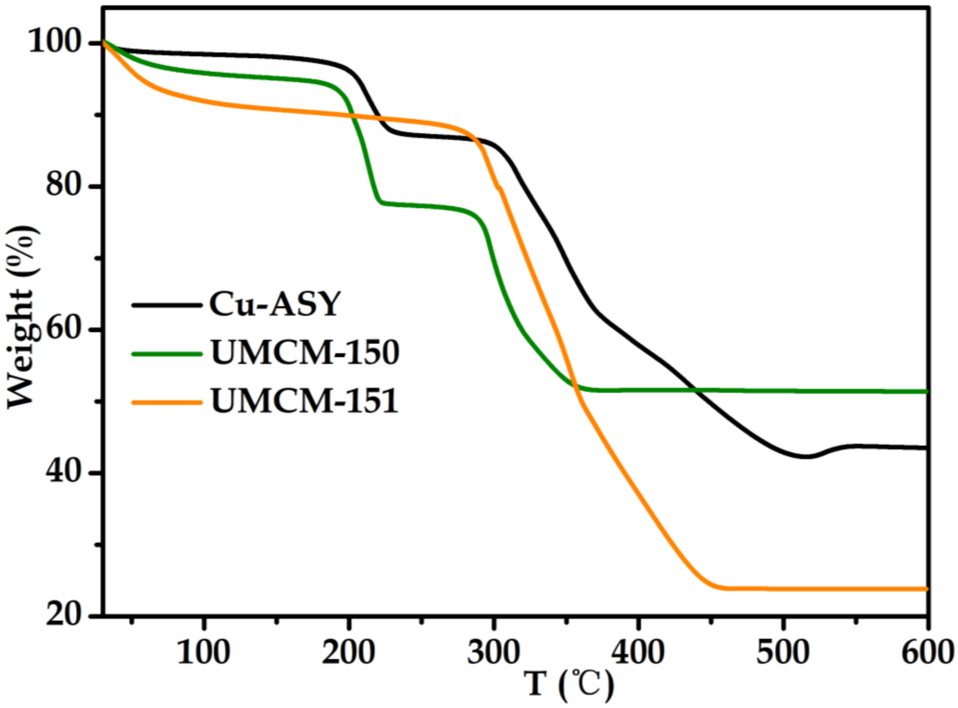

12. Figures S26-S28. Optical and SEM images

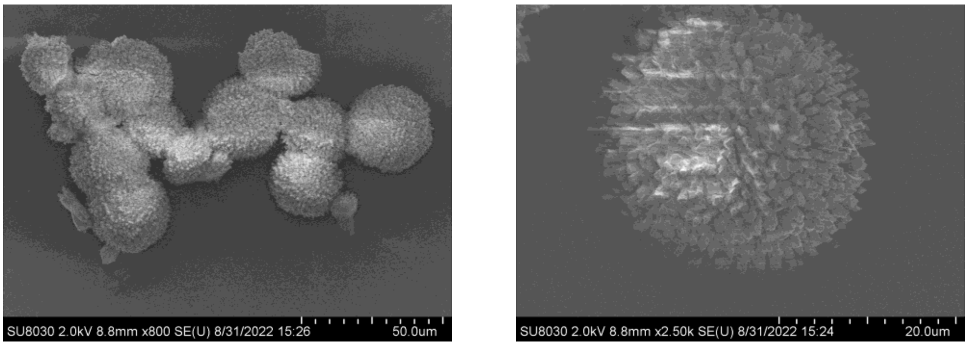

Figure S26. SEM images of Cu-ASY microcrystals

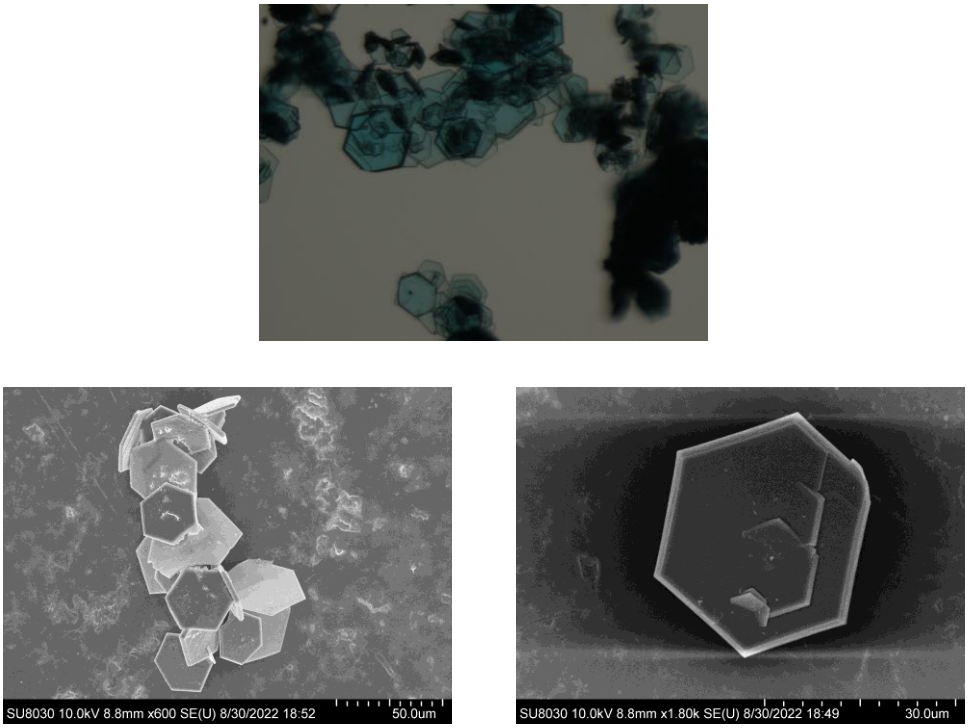

Figure S27. Optical (Top) and SEM images (bottom) of UMCM-150.

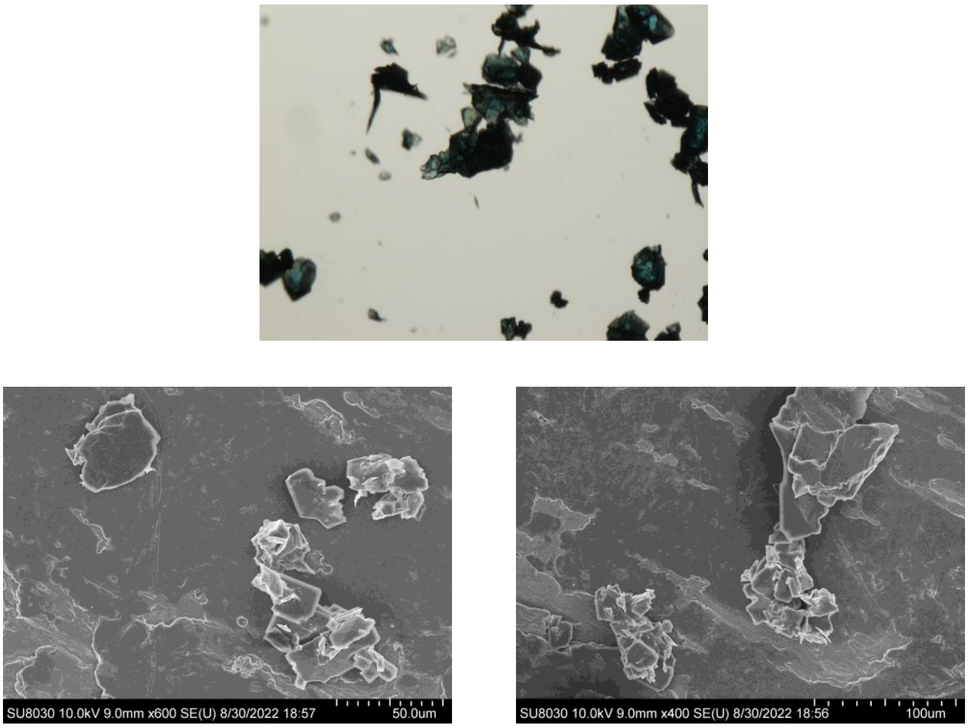

Figure S28 Optical (Top) and SEM images (bottom) of UMCM-151.

13. Figure S29. Comparison of C_3H_8/C_3H_6 separation selectivity

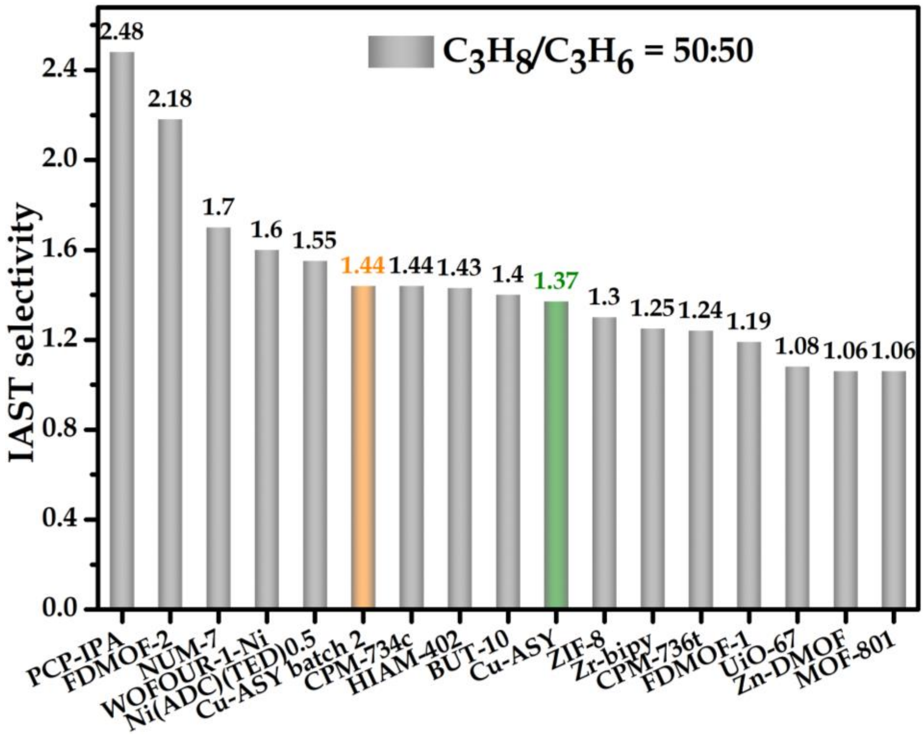

Figure S29. Comparison of inverse C_3H_8/C_3H_6 selectivity of Cu-ASY with other C_3H_8-selective materials.

14. Figure S30. SEM and EDS mapping images of Zn-ASY

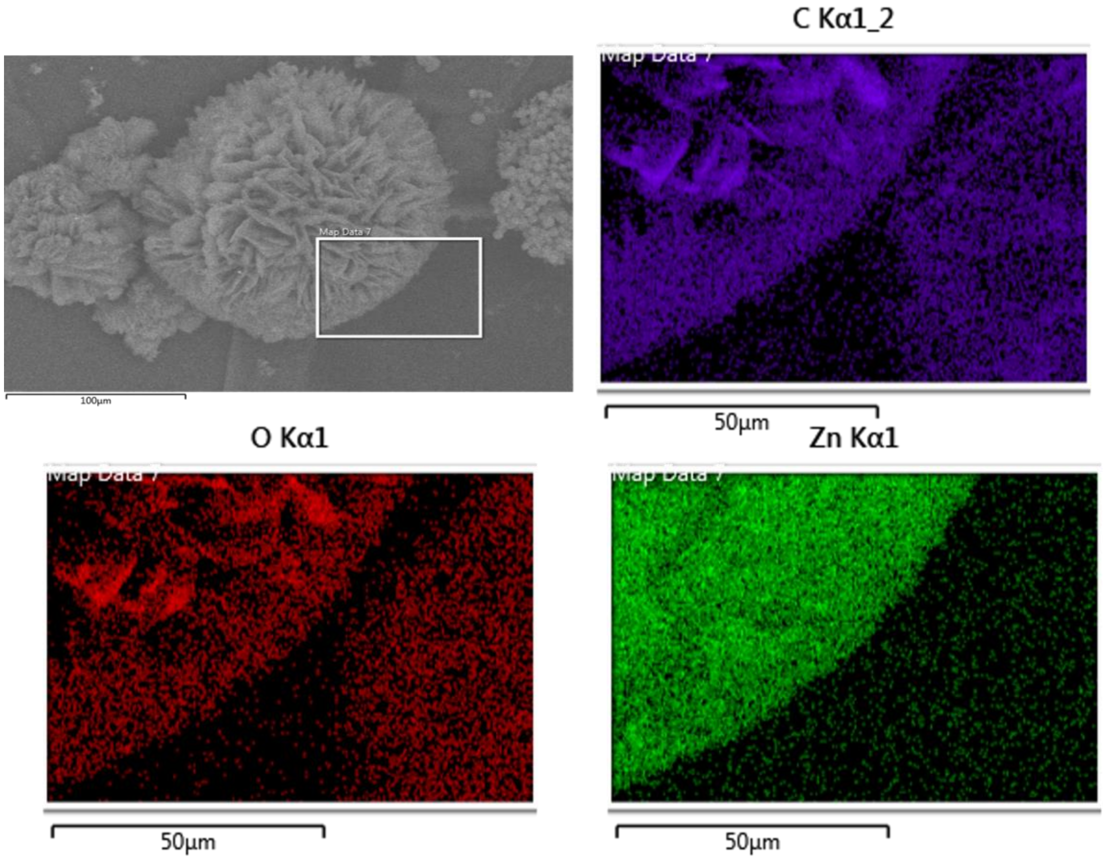

15. Figure S31. PXRD patterns of Zn-ASY and Cu-ASY

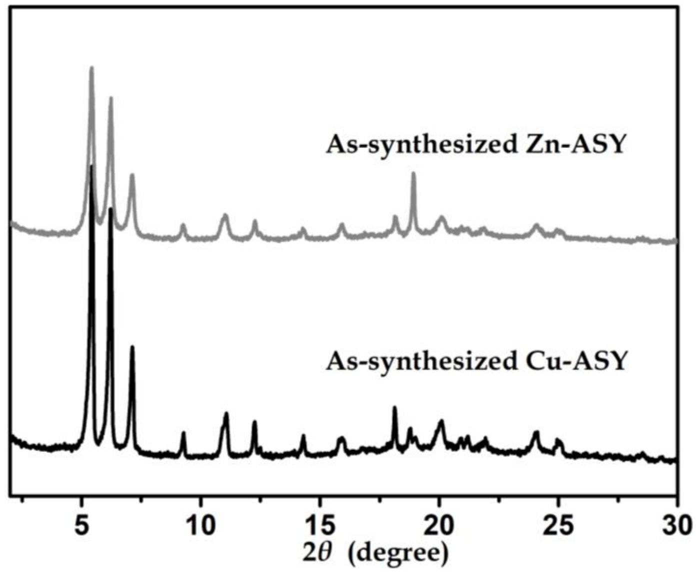

16. Figure S32. Derived 2D fingerprint plot of host-guest interactions in Cu-ASY

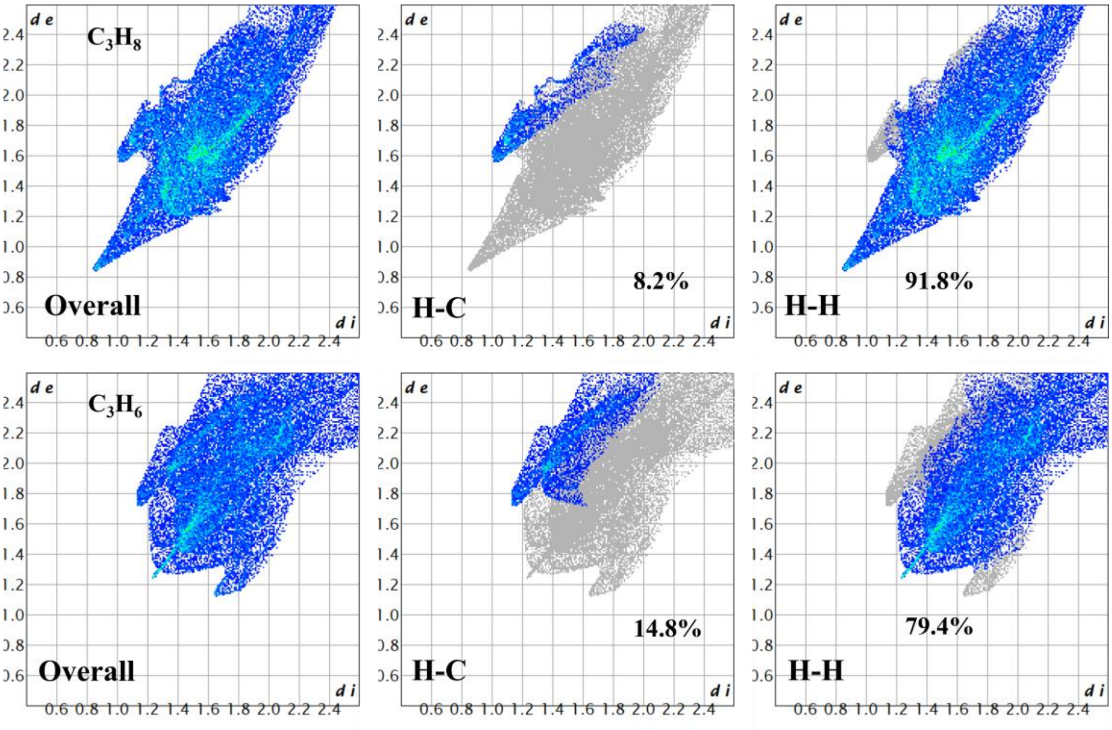

17. Figure S33. Comparison of C_3H_6 productivity

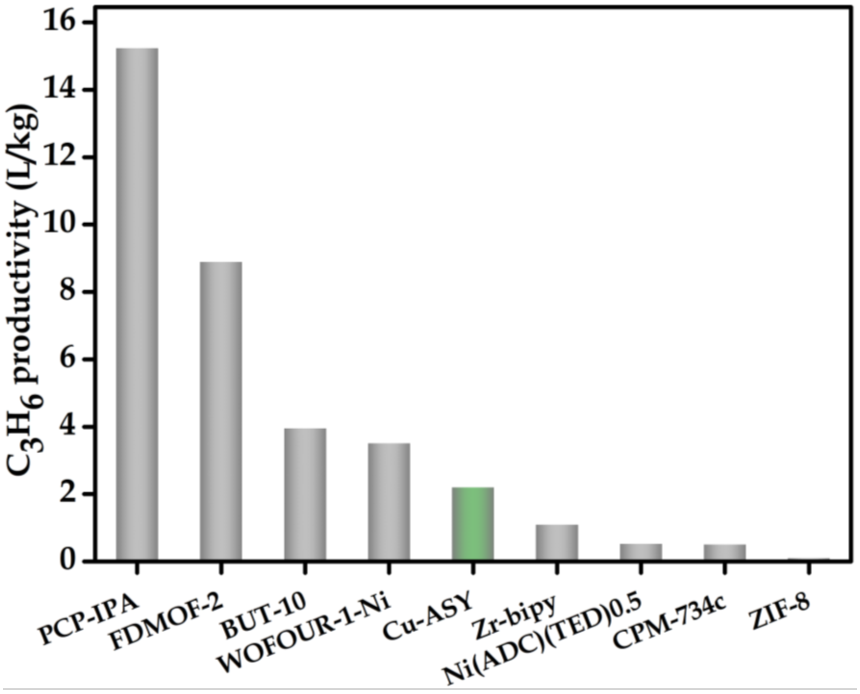

18. Figure S34. The PXRD patters of Cu-ASY after different treatments

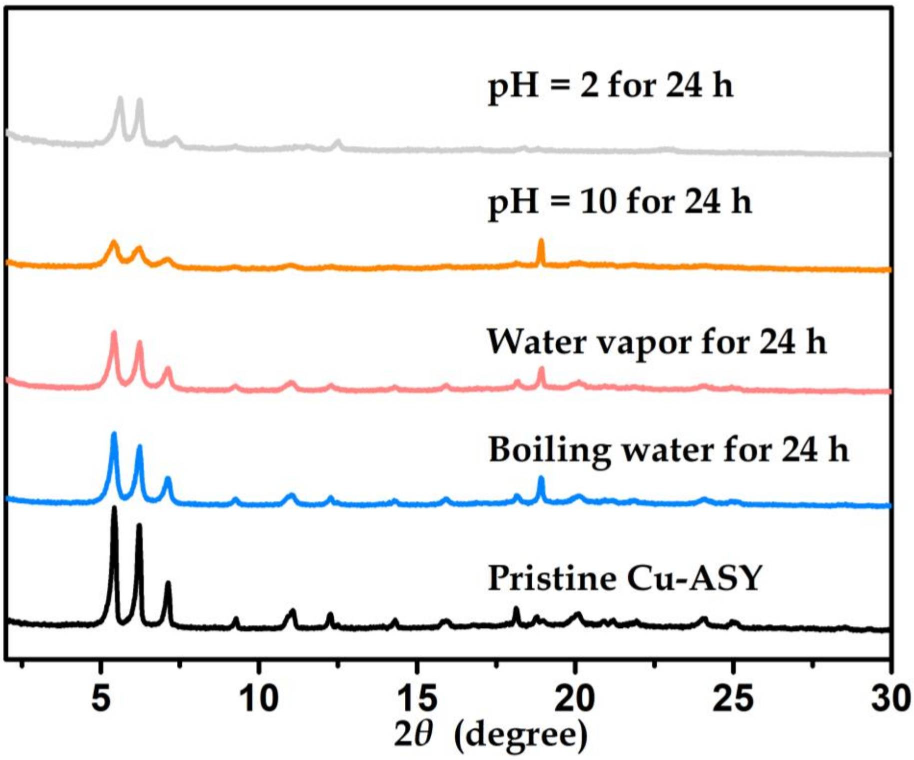

19. Figure S35. The sorption isotherms of C_2H_4 and C_2H_6 for Cu-ASY at 298 K

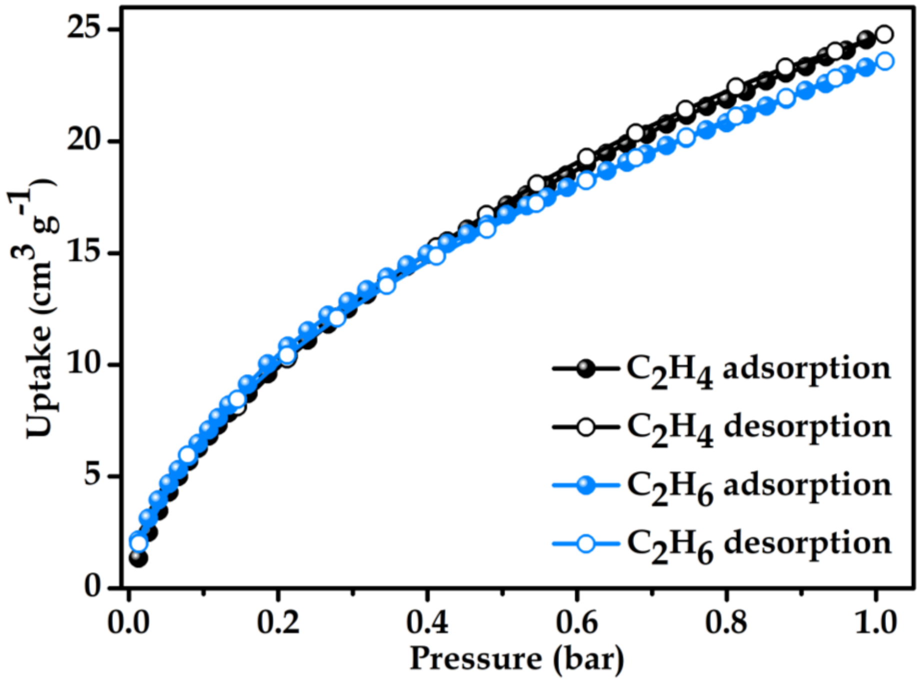

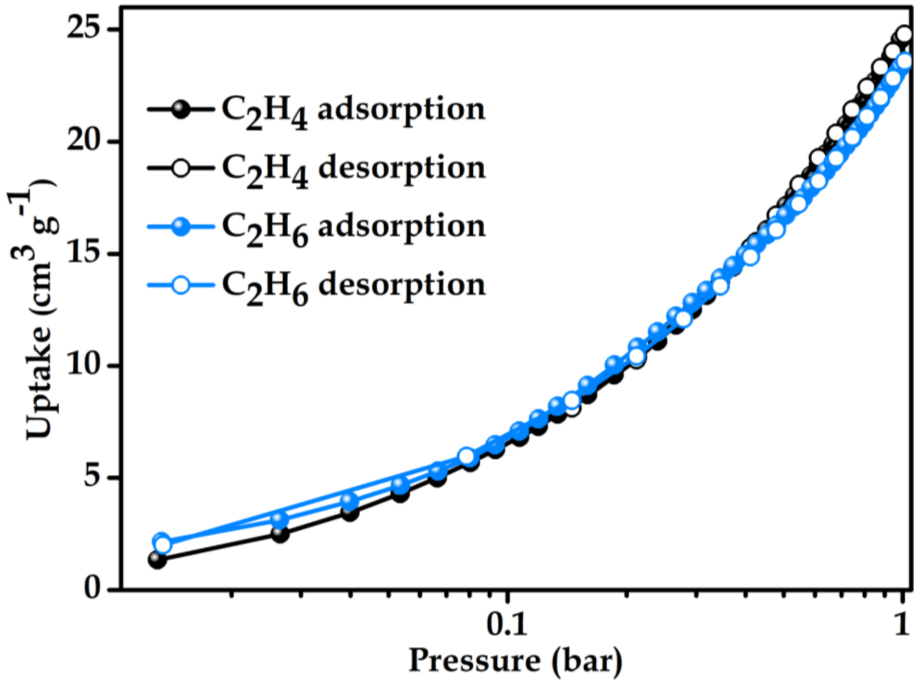

20. Figure S36. Water sorption isotherm of Cu-ASY at 298 K

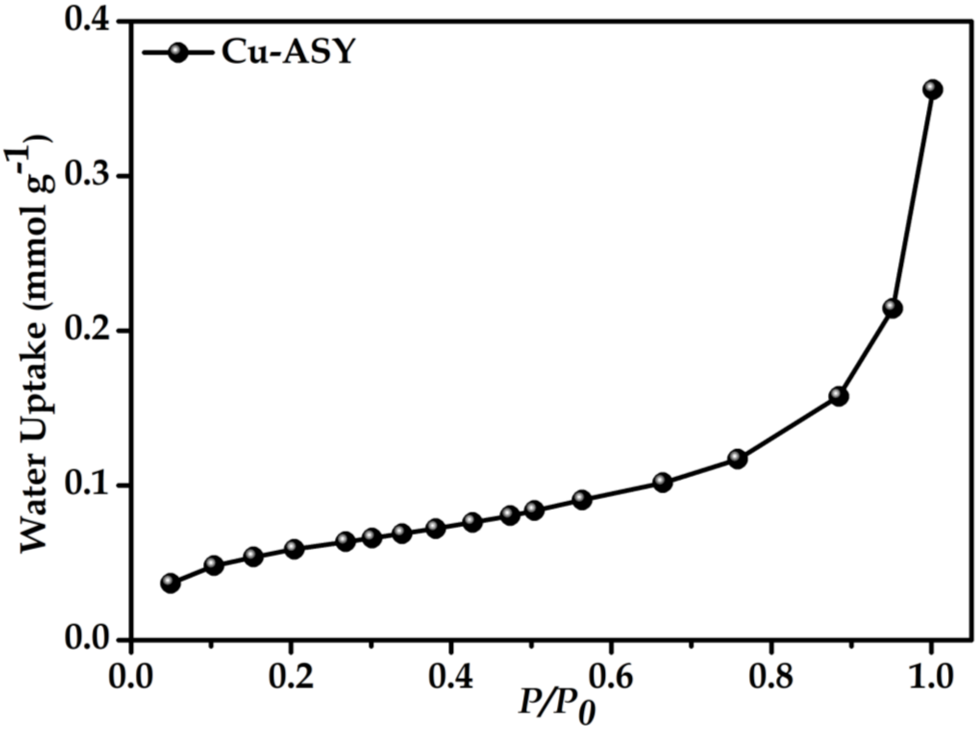

21. Figure S37. The breakthrough experiment of Cu-ASY under 30% RH

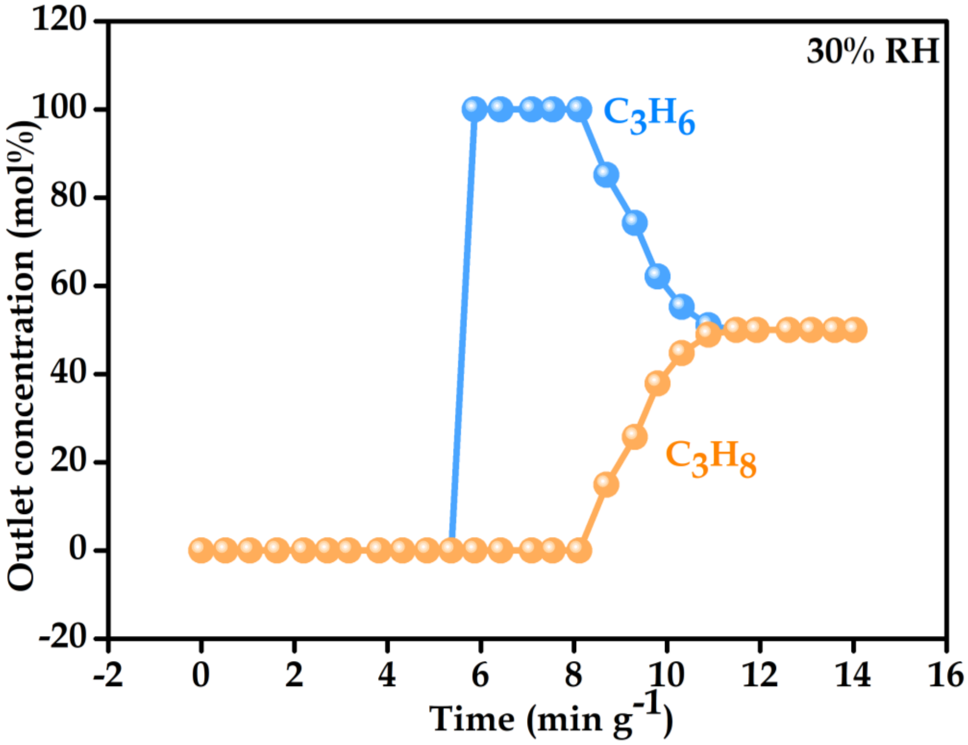

22. Figure S38. Structureless refinement (Le Bail) of the powder XRD data.

23. Figure S39. The fitting results of isotherms

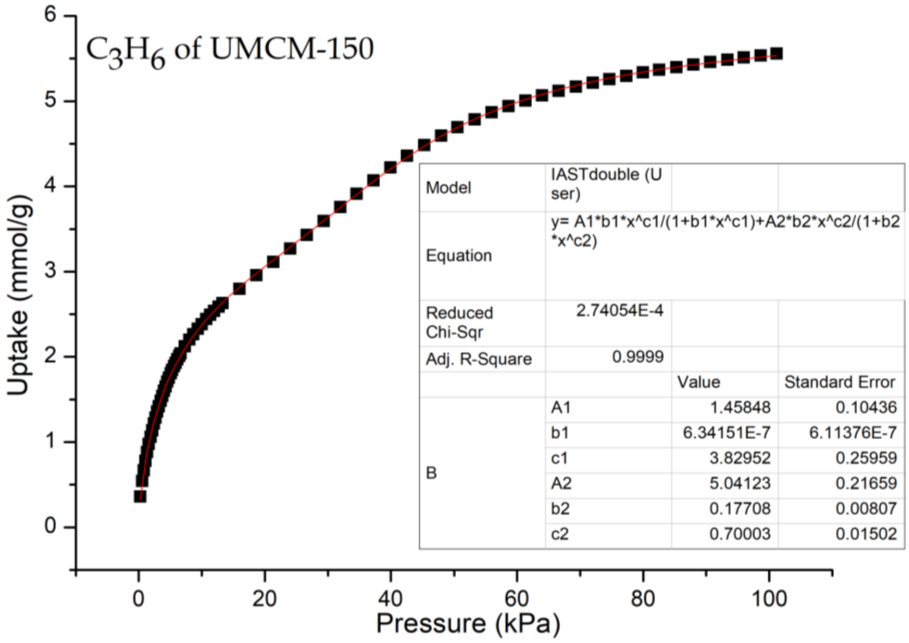

Model	IASTdouble (User)		
Equation	y= A1*b1*x^c1/(1+b1*x^c1)+A2*b2*x^c2/(1+b2*x^c2)		
Reduced Chi-Sqr	2.74054E-4		
Adj. R-Square	0.9999		
		Value	Standard Error
B	A1	1.45848	0.10436
	b1	6.34151E-7	6.11376E-7
	c1	3.82952	0.25959
	A2	5.04123	0.21659
	b2	0.17708	0.00807
	c2	0.70003	0.01502

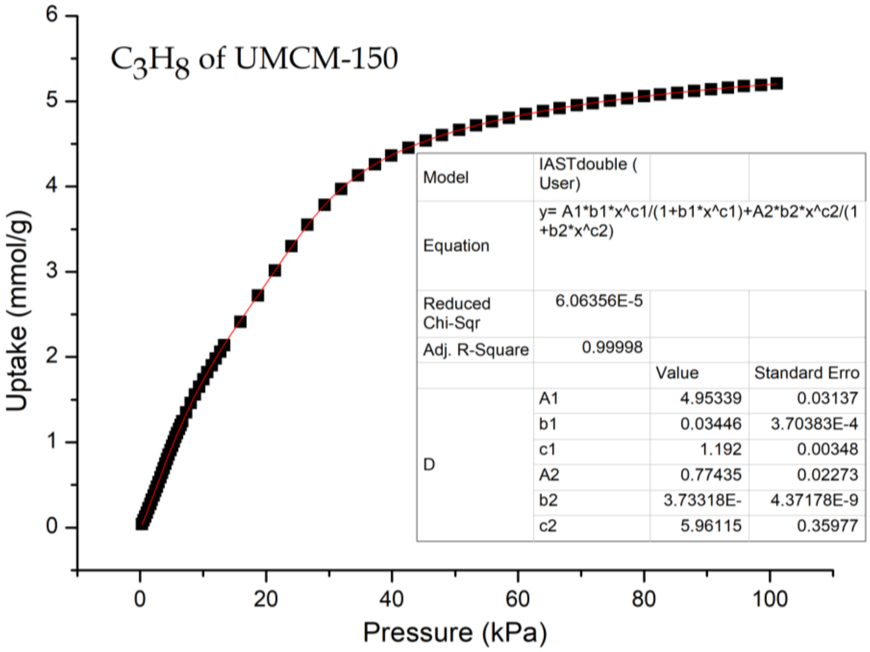

Model	IASTdouble (User)		
Equation	y= A1*b1*x^c1/(1+b1*x^c1)+A2*b2*x^c2/(1+b2*x^c2)		
Reduced Chi-Sqr	6.06356E-5		
Adj. R-Square	0.99998		
		Value	Standard Erro
D	A1	4.95339	0.03137
	b1	0.03446	3.70383E-4
	c1	1.192	0.00348
	A2	0.77435	0.02273
	b2	3.73318E-	4.37178E-9
	c2	5.96115	0.35977

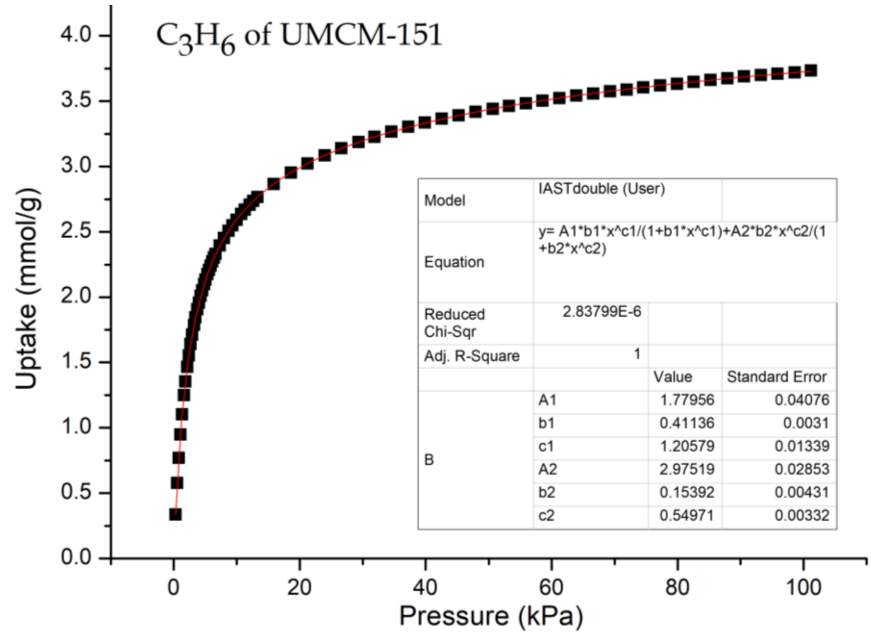

Model	IASTdouble (User)		
Equation	y= A1*b1*x^c1/(1+b1*x^c1)+A2*b2*x^c2/(1+b2*x^c2)		
Reduced Chi-Sqr	2.83799E-6		
Adj. R-Square	1		
		Value	Standard Error
B	A1	1.77956	0.04076
	b1	0.41136	0.0031
	c1	1.20579	0.01339
	A2	2.97519	0.02853
	b2	0.15392	0.00431
	c2	0.54971	0.00332

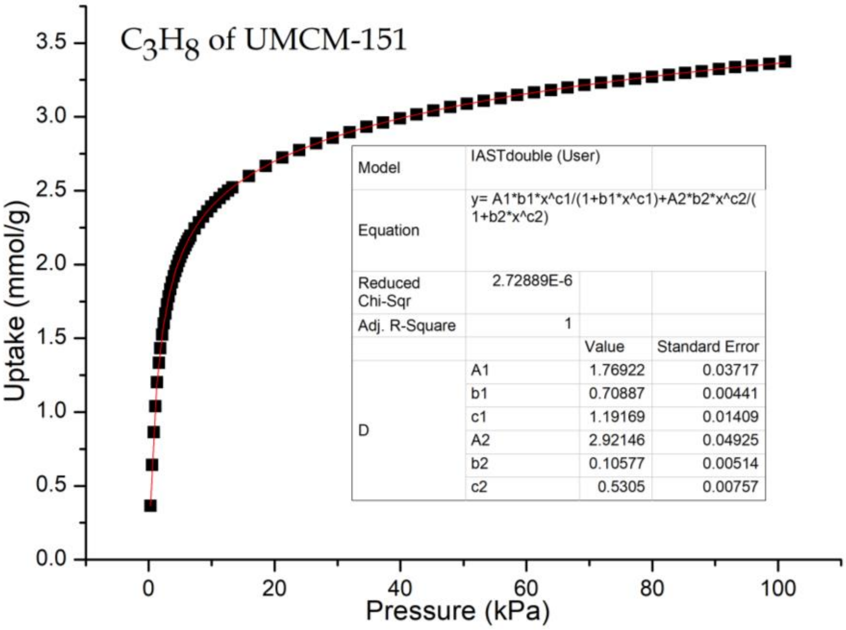

Model	IASTdouble (User)		
Equation	y= A1*b1*x^c1/(1+b1*x^c1)+A2*b2*x^c2/(1+b2*x^c2)		
Reduced Chi-Sqr	2.72889E-6		
Adj. R-Square	1		
		Value	Standard Error
D	A1	1.76922	0.03717
	b1	0.70887	0.00441
	c1	1.19169	0.01409
	A2	2.92146	0.04925
	b2	0.10577	0.00514
	c2	0.5305	0.00757

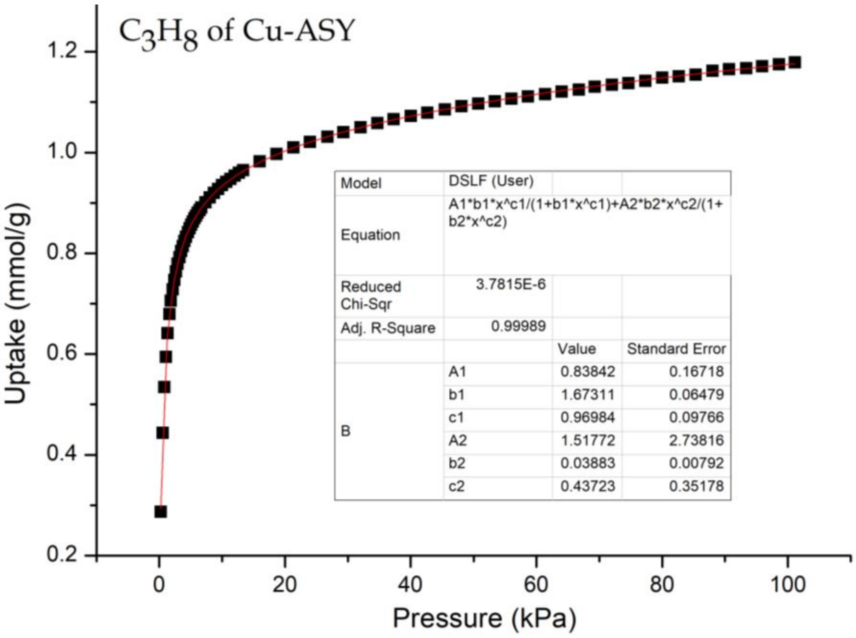

Model	DSLF (User)		
Equation	A1*b1*x^c1/(1+b1*x^c1)+A2*b2*x^c2/(1+b2*x^c2)		
Reduced Chi-Sqr	3.7815E-6		
Adj. R-Square	0.99989		
		Value	Standard Error
B	A1	0.83842	0.16718
	b1	1.67311	0.06479
	c1	0.96984	0.09766
	A2	1.51772	2.73816
	b2	0.03883	0.00792
	c2	0.43723	0.35178

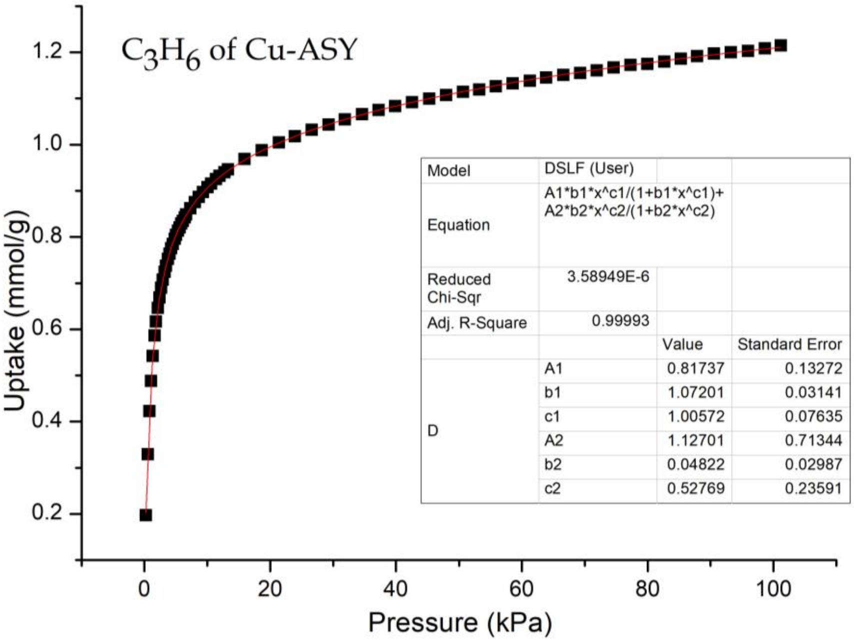

Model	DSLF (User)		
Equation	A1*b1*x^c1/(1+b1*x^c1)+A2*b2*x^c2/(1+b2*x^c2)		
Reduced Chi-Sqr	3.58949E-6		
Adj. R-Square	0.99993		
		Value	Standard Error
D	A1	0.81737	0.13272
	b1	1.07201	0.03141
	c1	1.00572	0.07635
	A2	1.12701	0.71344
	b2	0.04822	0.02987
	c2	0.52769	0.23591

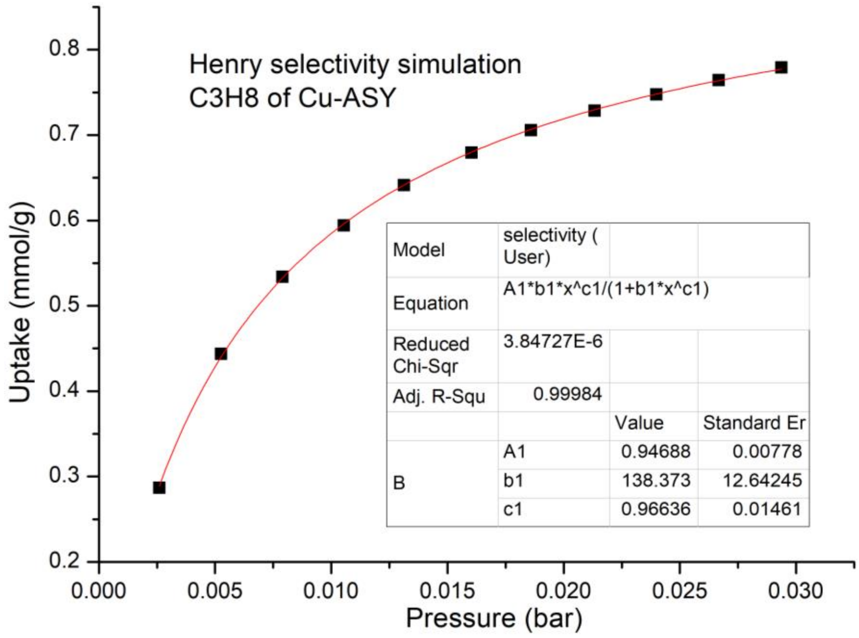

Model	selectivity (User)		
Equation	A1*b1*x^c1/(1+b1*x^c1)		
Reduced Chi-Sqr	3.84727E-6		
Adj. R-Squ	0.99984		
		Value	Standard Er
B	A1	0.94688	0.00778
	b1	138.373	12.64245
	c1	0.96636	0.01461

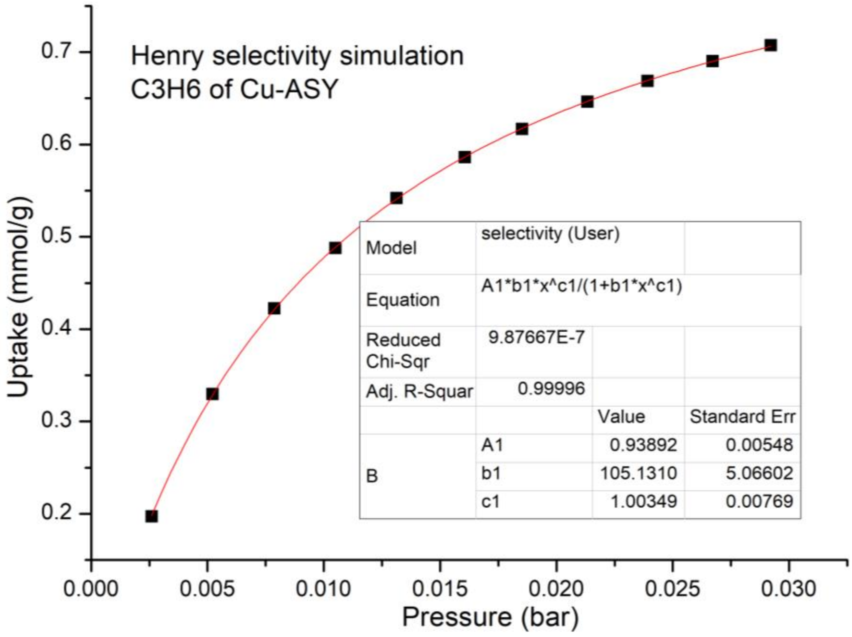

Model	selectivity (User)		
Equation	A1*b1*x^c1/(1+b1*x^c1)		
Reduced Chi-Sqr	9.87667E-7		
Adj. R-Squar	0.99996		
		Value	Standard Err
B	A1	0.93892	0.00548
	b1	105.1310	5.06602
	c1	1.00349	0.00769

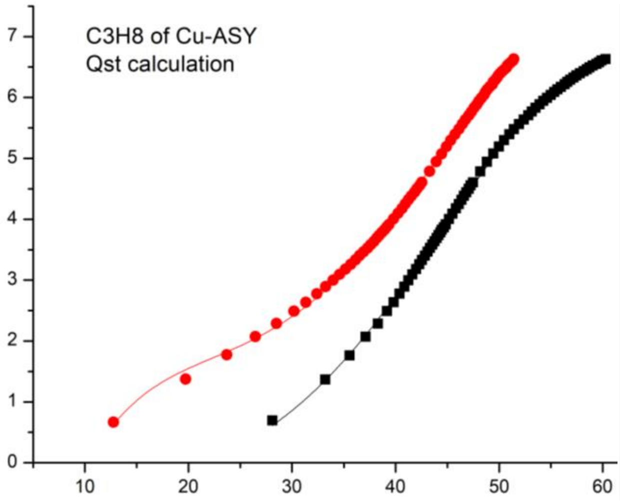

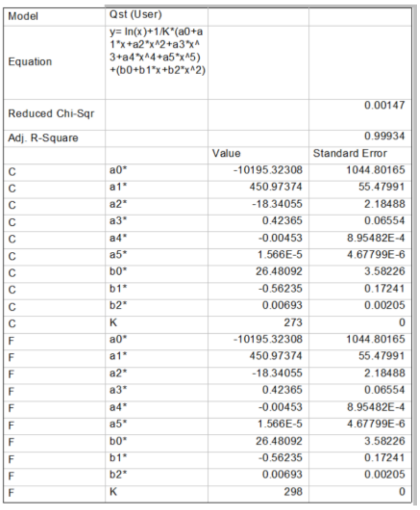

Model	Qst (User)		
Equation	y= ln(x)+1/K*(a0+a1*x+a2*x^2+a3*x^3+a4*x^4+a5*x^5)+(b0+b1*x+b2*x^2)		
Reduced Chi-Sqr			0.00147
Adj. R-Square			0.99934
		Value	Standard Error
C	a0*	-10195.32308	1044.80165
C	a1*	450.97374	55.47991
C	a2*	-18.34055	2.18488
C	a3*	0.42365	0.06554
C	a4*	-0.00453	8.95482E-4
C	a5*	1.566E-5	4.67799E-6
C	b0*	26.48092	3.58226
C	b1*	-0.56235	0.17241
C	b2*	0.00693	0.00205
C	K	273	0
F	a0*	-10195.32308	1044.80165
F	a1*	450.97374	55.47991
F	a2*	-18.34055	2.18488
F	a3*	0.42365	0.06554
F	a4*	-0.00453	8.95482E-4
F	a5*	1.566E-5	4.67799E-6
F	b0*	26.48092	3.58226
F	b1*	-0.56235	0.17241
F	b2*	0.00693	0.00205
F	K	298	0

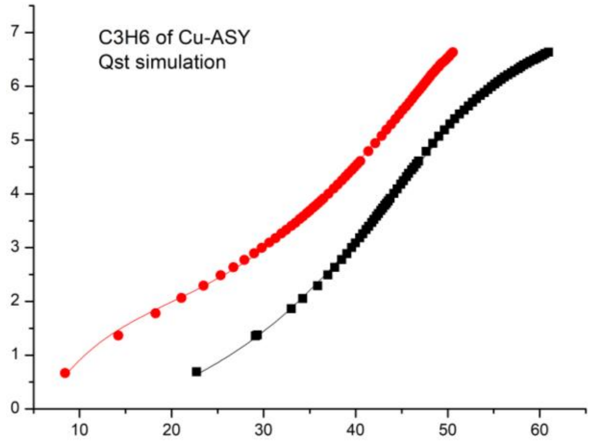

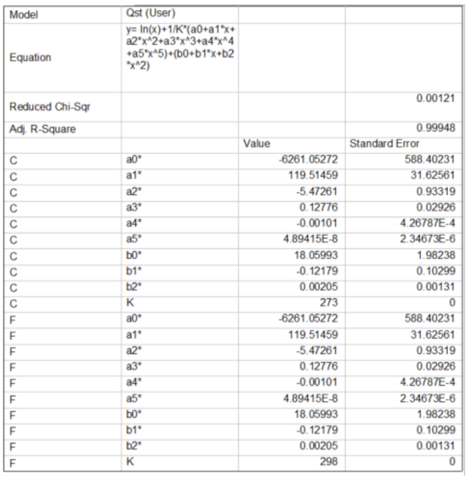

Model	Qst (User)		
Equation	y= ln(x)+1/K*(a0+a1*x+a2*x^2+a3*x^3+a4*x^4+a5*x^5)+(b0+b1*x+b2*x^2)		
Reduced Chi-Sqr			0.00121
Adj. R-Square			0.99948
		Value	Standard Error
C	a0*	-6261.05272	588.40231
C	a1*	119.51459	31.62561
C	a2*	-5.47261	0.93319
C	a3*	0.12776	0.02926
C	a4*	-0.00101	4.26787E-4
C	a5*	4.89415E-8	2.34673E-6
C	b0*	18.05993	1.98238
C	b1*	-0.12179	0.10299
C	b2*	0.00205	0.00131
C	K	273	0
F	a0*	-6261.05272	588.40231
F	a1*	119.51459	31.62561
F	a2*	-5.47261	0.93319
F	a3*	0.12776	0.02926
F	a4*	-0.00101	4.26787E-4
F	a5*	4.89415E-8	2.34673E-6
F	b0*	18.05993	1.98238
F	b1*	-0.12179	0.10299
F	b2*	0.00205	0.00131
F	K	298	0

References from main text with titles

(1) Cui, Y.; Li, B.; He, H.; Zhou, W.; Chen, B.; Qian, G. Metal-Organic Frameworks as Platforms for Functional Materials. *Acc. Chem. Res*. **2016,** *49*, 483-493.

(2) Furukawa, H.; Cordova, K. E.; O'Keeffe, M.; Yaghi, O. M. The Chemistry and Applications of Metal-Organic Frameworks. *Science* **2013,** *341*, 1230444.

(3) Gong, W.; Chen, Z.; Dong, J.; Liu, Y.; Cui, Y. Chiral Metal-Organic Frameworks. *Chem. Rev*. **2022,** *122*, 9078-9144.

(4) He, Y.; Li, B.; O'Keeffe, M.; Chen, B. Multifunctional Metal-Organic Frameworks Constructed from Meta-Benzenedicarboxylate Units. *Chem. Soc. Rev*. **2014,** *43*, 5618-5656.

(5) Kitagawa, S. Metal-Organic Frameworks (MOFs). *Chem. Soc. Rev*. **2014,** *43*, 5415-5418.

(6) Yaghi, O. M.; Kalmutzki, M. J.; Diercks, C. S. Introduction to Reticular Chemistry: Metal-Organic Frameworks and Covalent Organic Frameworks. John Wiley & Sons: **2019**.

(7) Alsadun, N.; Mouchaham, G.; Guillerm, V.; Czaban-Jóźwiak, J.; Shkurenko, A.; Jiang, H.; Bhatt, P. M.; Parvatkar, P.; Eddaoudi, M. Introducing a Cantellation Strategy for the Design of Mesoporous Zeolite-Like Metal-Organic Frameworks: Zr-Sod-ZMOFs as a Case Study. *J. Am. Chem. Soc*. **2020,** *142*, 20547-20553.

(8) Eddaoudi, M.; Sava, D. F.; Eubank, J. F.; Adil, K.; Guillerm, V. Zeolite-Like Metal-Organic Frameworks (ZMOFs): Design, Synthesis, and Properties. *Chem. Soc. Rev*. **2015,** *44*, 228-249.

(9) Inge, A. K.; Köppen, M.; Su, J.; Feyand, M.; Xu, H.; Zou, X.; O'Keeffe, M.; Stock, N. Unprecedented Topological Complexity in a Metal-Organic Framework Constructed from Simple Building Units. *J. Am. Chem. Soc*. **2016,** *138*, 1970-1976.

(10) Skorupskii, G.; Dincă, M. Electrical Conductivity in a Porous, Cubic Rare-Earth Catecholate. *J. Am. Chem. Soc*. **2020,** *142*, 6920-6924.

(11) Tian, D.; Chen, Q.; Li, Y.; Zhang, Y. H.; Chang, Z.; Bu, X. H. A Mixed Molecular Building Block Strategy for the Design of Nested Polyhedron Metal-Organic Frameworks. *Angew. Chem. Int. Ed*. **2014,** *126*, 856-860.

(12) Jiang, H.; Alezi, D.; Eddaoudi, M. A Reticular Chemistry Guide for the Design of Periodic Solids. *Nat. Rev. Mater*. **2021,** *6*, 466-487.

(13) Kampouri, S.; Zhang, M.; Chen, T.; Oppenheim, J. J.; Brown, A. C.; Payne, M. T.; Andrews, J. L.; Sun, J.; Dincă, M. Pyrogallate-Based Metal-Organic Framework with a Two Dimensional Secondary Building Unit. *Angew. Chem. Int. Ed*. **2022,** *134*, e202213960.

(14) Rosi, N. L.; Kim, J.; Eddaoudi, M.; Chen, B.; O'Keeffe, M.; Yaghi, O. M. Rod Packings and Metal-Organic Frameworks Constructed from Rod-Shaped Secondary Building Units. *J. Am. Chem. Soc*. **2005,** *127,* 1504-1518.

(15) Schoedel, A.; Li, M.; Li, D.; O'Keeffe, M.; Yaghi, O. M. Structures of Metal-Organic Frameworks with Rod Secondary Building Units. *Chem. Rev*. **2016,** *116*, 12466-12535.

(16) Zhang, Y.-F.; Zhang, Z.-H.; Ritter, L.; Fang, H.; Wang, Q.; Space, B.; Zhang, Y.-B.; Xue, D.-X.; Bai, J. New Reticular Chemistry of the Rod Secondary Building Unit: Synthesis, Structure, and Natural Gas Storage of a Series of Three-Way Rod Amide-Functionalized Metal-Organic Frameworks. *J. Am. Chem. Soc*. **2021,** *143*, 12202-12211.

(17) Zhao, X.; Shimazu, M. S.; Chen, X.; Bu, X.; Feng, P. Homo-Helical Rod Packing as a Path toward the Highest Density of Guest-Binding Metal Sites in Metal-Organic Frameworks. *Angew. Chem. Int. Ed*. **2018,** *57*, 6208-6211.

(18) Cui, H.; Ye, Y.; Lin, R.; Shi, Y.; Alothman, Z. A.; Alduhaish, O.; Wang, B.; Zhang, J.; Chen, B. An Indium-Based Microporous Metal-Organic Framework with Unique Three-Way Rod-Shaped Secondary Building Units for Efficient Methane and Hydrogen Storage. *Inorg. Chem. Front*. **2022,** *9*, 6527-6533.

(19) Moribe, S.; Chen, Z.; Alayoglu, S.; Syed, Z. H.; Islamoglu, T.; Farha, O. K. Ammonia Capture within Isoreticular Metal-Organic Frameworks with Rod Secondary Building Units. *ACS Materials Lett*. **2019,** *1*, 476-480.

(20) Barthelet, K.; Marrot, J.; Riou, D.; Férey, G. A Breathing Hybrid Organic-Inorganic Solid with Very Large Pores and High Magnetic Characteristics. *Angew. Chem. Int. Ed*. **2002,** *41*, 281-284.

(21) Serre, C.; Millange, F.; Thouvenot, C.; Noguès, M.; Marsolier, G.; Louër, D.; Férey, G. Very Large Breathing Effect in the First Nanoporous Chromium (III)-Based Solids: MIL-53 or $Cr^{III}(OH)\cdot\{O_2C-C_6H_4-CO_2\}\cdot\{HO_2C-C_6H_4-CO_2H\}_x\cdot H_2O_y$. *J. Am. Chem. Soc*. **2002,** *124*, 13519-13526.

(22) Yang, S.; Ramirez-Cuesta, A. J.; Newby, R.; Garcia-Sakai, V.; Manuel, P.; Callear, S. K.; Campbell, S. I.; Tang, C. C.; Schröder, M. Supramolecular Binding and Separation of Hydrocarbons within a Functionalized Porous Metal-Organic Framework. *Nat. Chem*.**2015,** *7*, 121-129.

(23) Deng, H.; Grunder, S.; Cordova, K. E.; Valente, C.; Furukawa, H.; Hmadeh, M.; Gándara, F.; Whalley, A. C.; Liu, Z.; Asahina, S.; Kazumori, H.; O'Keeffe, M.; Terasaki, O.; Stoddart, J. F.; Yaghi, O. M. Large-Pore Apertures in a Series of Metal-Organic Frameworks. *Science* **2012,** *336*, 1018-1023.

(24) Flaig, R. W.; Osborn Popp, T. M.; Fracaroli, A. M.; Kapustin, E. A.; Kalmutzki, M. J.; Altamimi, R. M.; Fathieh, F.; Reimer, J. A.; Yaghi, O. M. The Chemistry of CO_2

Capture in an Amine-Functionalized Metal-Organic Framework under Dry and Humid Conditions. *J. Am. Chem. Soc*. **2017,** *139*, 12125-12128.

(25) Han, Z.; Wang, K.; Min, H.; Xu, J.; Shi, W.; Cheng, P. Bifunctionalized Metal-Organic Frameworks for Pore-Size-Dependent Enantioselective Sensing. *Angew. Chem. Int. Ed*. **2022,** *61*, e202204066.

(26) Peng, S.; Bie, B.; Sun, Y.; Liu, M.; Cong, H.; Zhou, W.; Xia, Y.; Tang, H.; Deng, H.; Zhou, X. Metal-Organic Frameworks for Precise Inclusion of Single-Stranded DNA and Transfection in Immune Cells. *Nat. Commun*. **2018,** *9*, 1293.

(27) Catarineu, N. R.; Schoedel, A.; Urban, P.; Morla, M. B.; Trickett, C. A.; Yaghi, O. M. Two Principles of Reticular Chemistry Uncovered in a Metal-Organic Framework of Heterotritopic Linkers and Infinite Secondary Building Units. *J. Am. Chem. Soc*. **2016,** *138*, 10826-10829.

(28) Lv, X.-L.; Feng, L.; Xie, L.-H.; He, T.; Wu, W.; Wang, K.-Y.; Si, G.; Wang, B.; Li, J.-R.; Zhou, H.-C. Linker Desymmetrization: Access to a Series of Rare-Earth Tetracarboxylate Frameworks with Eight-Connected Hexanuclear Nodes. *J. Am. Chem. Soc*. **2021,** *143*, 2784-2791.

(29) Sun, J.; Zhang, X.; Zhang, D.; Chen, Y.-P.; Wang, F.; Li, L.; Liu, T.-F.; Yang, H.; Song, J.; Cao, R. Building Block Symmetry Relegation Induces Mesopore and Abundant Open-Metal Sites in Metal-Organic Frameworks for Cancer Therapy. *CCS Chem*. **2022,** *4*, 996-1006.

(30) Wang, Y.; Liu, Z.; Li, Y.; Bai, Z.; Liu, W.; Wang, Y.; Xu, X.; Xiao, C.; Sheng, D.; Diwu, J.; Su, J.; Chai, Z.; Albrecht-Schmitt, T. E.; Wang, S. Umbellate Distortions of the Uranyl Coordination Environment Result in a Stable and Porous Polycatenated Framework That Can Effectively Remove Cesium from Aqueous Solutions. *J. Am. Chem. Soc*. **2015,** *137*, 6144-6147.

(31) Yu, L.; Ullah, S.; Zhou, K.; Xia, Q.; Wang, H.; Tu, S.; Huang, J.; Xia, H.-L.; Liu, X.-Y.; Thonhauser, T.; Li, J. A Microporous Metal-Organic Framework Incorporating Both Primary and Secondary Building Units for Splitting Alkane Isomers. *J. Am. Chem. Soc*. **2022,** *144*, 3766-3770.

(32) Guillerm, V.; Maspoch, D. Geometry Mismatch and Reticular Chemistry: Strategies to Assemble Metal-Organic Frameworks with Non-Default Topologies. *J. Am. Chem. Soc*. **2019,** *141*, 16517-16538.

(33) Chui, S. S.-Y.; Lo, S. M.-F.; Charmant, J. P. H; Orpen, A. G.; Williams, I. D. A Chemically Functionalizable Nanoporous Material $[Cu_3(TMA)_2(H_2O)_3]_n$. *Science* **1999,** *283*, 1148-1150.

(34) Férey, G.; Serre, C.; Mellot-Draznieks, C.; Millange, F.; Surblé, S.; Dutour, J.; Margiolaki, I. A Hybrid Solid with Giant Pores Prepared by a Combination of Targeted Chemistry, Simulation, and Powder Diffraction. *Angew. Chem. Int. Ed*. **2004,** *116*, 6456-6461.

(35) Furukawa, H.; Gandara, F.; Zhang, Y.-B.; Jiang, J.; Queen, W. L.; Hudson, M. R.; Yaghi, O. M. Water Adsorption in Porous Metal-Organic Frameworks and Related Materials. *J. Am. Chem. Soc*. **2014,** *136*, 4369-4381.

(36) Chen, Y.; Zhang, X.; Ma, K.; Chen, Z.; Wang, X.; Knapp, J.; Alayoglu, S.; Wang, F.; Xia, Q.; Li, Z.; Islamoglu, T.; Farha, O. K. Zirconium-Based Metal-Organic

Framework with 9-Connected Nodes for Ammonia Capture. *ACS Appl. Nano Mater*. **2019,** *2*, 6098-6102.

(37) Feng, D.; Wang, K.; Su, J.; Liu, T. F.; Park, J.; Wei, Z.; Bosch, M.; Yakovenko, A.; Zou, X.; Zhou, H. C. A Highly Stable Zeotype Mesoporous Zirconium Metal-Organic Framework with Ultralarge Pores. *Angew. Chem. Int. Ed*. **2015,** *54*, 149-154.

(38) Schnobrich, J. K.; Lebel, O.; Cychosz, K. A.; Dailly, A.; Wong-Foy, A. G.; Matzger, A. Linker-Directed Vertex Desymmetrization for the Production of Coordination Polymers with High Porosity. *J. Am. Chem. Soc*. **2010,** *132*, 13941-13948.

(39) Wong-Foy, A. G.; Lebel, O.; Matzger, A. Porous Crystal Derived from a Tricarboxylate Linker with Two Distinct Binding Motifs. *J. Am. Chem. Soc*. **2007,** *129*, 15740-15741.

(40) Barnard, R. A.; Dutta, A.; Schnobrich, J. K.; Morrison, C. N.; Ahn, S.; Matzger, A. Two-Dimensional Crystals from Reduced Symmetry Analogues of Trimesic Acid. *Chem. Eur. J*. **2015,** *21*, 5954-5961.

(41) Blatov, V. A.; Shevchenko, A. P.; Proserpio, D. M. Applied Topological Analysis of Crystal Structures with the Program Package Topospro. *Cryst. Growth Des*. **2014,** *14*, 3576-3586.

(42) Koch, E.; Fischer, W. Types of Sphere Packings for Crystallographic Point Groups, Rod Groups and Layer Groups. *Z. Kristallogr. Cryst. Mater*. **1978**, *148*, 107-152.

(43) O'Keeffe, M.; Peskov, M. A.; Ramsden, S. J.; Yaghi, O. M. The Reticular Chemistry Structure Resource (RCSR) Database of, and Symbols for, Crystal Nets. *Acc. Chem. Res*. **2008,** *41*, 1782-1789.

(44) Blatov, V.; O'Keeffe, M.; Proserpio, D. M. Vertex-, Face-, Point-, SchläFli-, and Delaney-Symbols in Nets, Polyhedra and Tilings: Recommended Terminology. *CrystEngComm*. **2010,** *12*, 44-48.

(45) Xie, L. S.; Alexandrov, E. V.; Skorupskii, G.; Proserpio, D. M.; Dincă, M. Diverse π–π Stacking Motifs Modulate Electrical Conductivity in Tetrathiafulvalene-Based Metal-Organic Frameworks. *Chem. Sci*. **2019,** *10*, 8558-8565.

(46) Wang, X.; Li, T.; Li, L.; Lin, R. B.; Jia, X.; Chang, Z.; Wen, H. M.; Chen, X.; Li, J. Construction of Fluorinated Propane-Trap in Metal–Organic Frameworks for Record Polymer-Grade Propylene Production under High Humidity Conditions. *Adv. Mater*. **2023**, *35*, 2207955.

(47) Zhang, P.; Yang, L.; Liu, X.; Wang, J.; Suo, X.; Chen, L.; Cui, X.; Xing, H. Ultramicroporous Material Based Parallel and Extended Paraffin Nano-Trap for Benchmark Olefin Purification. *Nat. Commun*. **2022**, *13*, 4928.

(48) L. Yang, X. Cui, Q. Ding, Q. Wang, A. Jin, L. Ge, H. Xing, Polycatenated Molecular Cage-Based Propane Trap for Propylene Purification with Recorded Selectivity. ACS Appl. Mater. Interfaces 2020, 12, 2525.

(49) Spackman, P. R.; Turner, M. J.; McKinnon, J. J.; Wolff, S. K.; Grimwood, D. J.; Jayatilaka, D.; Spackman, M. A. CrystalExplorer: a Program for Hirshfeld Surface Analysis, Visualization and Quantitative Analysis of Molecular Crystals. *J. Appl. Crystallogr.* **2021**, *54*, 1006-1011.